EFFECT OF THICKNESS-TO-CHORD RATIO ON FLOW STRUCTURE OF A LOW SWEPT DELTA WING

A THESIS SUBMITTED TO
THE GRADUATE SCHOOL OF NATURAL AND APPLIED SCIENCES
OF
MIDDLE EAST TECHNICAL UNIVERSITY

BY

BURAK GÜLSAÇAN

IN PARTIAL FULFILLMENT OF THE REQUIREMENTS
FOR
THE DEGREE OF MASTER OF SCIENCE
IN
MECHANICAL ENGINEERING

SEPTEMBER 2017

Approval of the thesis:

EFFECT OF THICKNESS-TO-CHORD RATIO ON FLOW STRUCTURE OF A LOW SWEPT DELTA WING

submitted by **BURAK GÜLSAÇAN** in partial fulfillment of the requirements for the degree of **Master of Science in Mechanical Engineering Department, Middle East Technical University** by,

Prof. Dr. Gülbin Dural Ünver _____
Dean, Graduate School of **Natural and Applied Sciences**

Prof. Dr. Mehmet Ali Sahir Arıkan _____
Head of Department, **Mechanical Engineering**

Assoc. Prof. Dr. Mehmet Metin Yavuz _____
Supervisor, **Mechanical Engineering Dept., METU**

Examining Committee Members:

Assoc. Prof. Dr. Cüneyt Sert _____
Mechanical Engineering Dept., METU

Assoc. Prof. Dr. Mehmet Metin Yavuz _____
Mechanical Engineering Dept., METU

Asst. Prof. Dr. Feyza Kazanç _____
Mechanical Engineering Dept., METU

Asst. Prof. Dr. Ali Emre Turgut _____
Mechanical Engineering Dept., METU

Asst. Prof. Dr. Ekin Özgirgin Yapıcı _____
Mechanical Engineering Dept., Çankaya University

Date: 07.09.2017

I hereby declare that all information in this document has been obtained and presented in accordance with academic rules and ethical conduct. I also declare that, as required by these rules and conduct, I have fully cited and referenced all material and results that are not original to this work.

Name, Last name: Burak GÜLSAÇAN

Signature :

ABSTRACT

EFFECT OF THICKNESS-TO-CHORD RATIO ON FLOW STRUCTURE OF A LOW SWEPT DELTA WING

Gülsaçan, Burak
M.S., Department of Mechanical Engineering
Supervisor: Assoc. Prof. Dr. Mehmet Metin Yavuz

September 2017, 89 pages

Low swept delta wings, which are the simplified planforms of Unmanned Air Vehicles (UAVs), Unmanned Combat Air Vehicles (UCAVs) and Micro Air Vehicles (MAVs), have drawn considerable attention in recent years. In order to characterize and improve the operational parameters of these vehicles, the flow physics over low swept delta wings and its control should be well understood.

In literature, the effect of thickness-to-chord ratio (t/C) on aerodynamic performance of a delta wing was studied on high and moderate swept delta wings, whereas no attention has been paid on the effect of t/C ratio on global flow structure of low swept delta wings.

In the present study, the effect of t/C ratio on flow structure of a delta wing with sweep angle of 35 degree is characterized in a low speed wind tunnel using laser illuminated smoke visualization, near surface and cross-flow particle image velocimetry, and surface pressure measurements. Four delta wing models with t/C

ratio varying from 4.75 % to 19 % are tested at angles of attack varying from 4 to 10 degrees for Reynolds numbers Re=10,000 and 35,000.

The results indicate that the effect of thickness-to-chord ratio on flow structure is quite substantial, such that, as the wing thickness increases, the flow structure transforms from leading edge vortex to three-dimensional separated flow regime. The wing with low t/C ratio of 4.75 % experiences pronounced surface separation at significantly higher angle of attack compared to the wing with high t/C ratio. The results might explain some of the discrepancies reported in previously conducted studies related to delta wings. In addition, it is observed that the thickness of the shear layer separated from windward side of the wing is directly correlated with the thickness of the wing. To conclude, the flow structure on low swept delta wing is highly affected by t/C ratio, which in turn might indicate the potential usage of wing thickness as an effective flow control parameter.

Keywords: Delta wing, low sweep, three dimensional surface separation, wing thickness, thickness-to-chord ratio.

ÖZ

KALINLIK-VETER ORANININ DÜŞÜK OK AÇILI DELTA KANAT ÜZERİNDEKİ AKIŞ YAPISINA ETKİSİ

Gülsaçan, Burak
Yüksek Lisans, Makina Mühendisliği Bölümü
Tez Yöneticisi : Doç. Dr. Mehmet Metin Yavuz

Eylül 2017, 89 sayfa

İnsansız Hava Araçları (UAV'ler), İnsansız Savaş Hava Araçları (UCAV'ler) ve Mikro Hava Araçlarının (MAV'ler) basitleştirilmiş plan biçimleri olan düşük ok açılı delta kanatlar, son yıllarda büyük ilgi görmektedir. Bu araçların operasyonel parametrelerini karakterize etmek ve geliştirmek için, düşük ok açılı delta kanatlar üzerindeki akış fiziği ve kontrolü iyi anlaşılmalıdır.

Literatürde bir delta kanadın aerodinamik performansı üzerindeki kalınlık-veter oranının (t / C) etkisi, yüksek ve orta düzeyde ok açılı delta kanatlar üzerinde incelenirken, t / C oranının düşük ok açılı delta kanatların genel akış yapısı üzerindeki etkisine hiç dikkat edilmemiştir.

Bu çalışmada, 35 ° 'lik ok açısına sahip bir delta kanadın akış yapısı üzerindeki t / C oranının etkisi, lazer aydınlatmalı duman görüntüleme, yakın-yüzey ve çapraz akış parçacık görüntülemeli hız ölçüm ve yüzey basınç ölçüm teknikleri kullanılarak düşük hızlı bir rüzgar tünelinde karakterize edilmiştir. t / C oranı %

4.75 ila % 19 arasında değişen dört delta kanat modeli, Reynolds sayısı Re = 10.000 ve 35.000 için 4 ile 10 derece aralığındaki atak açılarında test edilmiştir.

Sonuçlar, kanat kalınlığı arttıkça akış yapısının hücum kenarı girdabından üç boyutlu yüzeyden ayrılmış akış rejimine dönüşecek şekilde kalınlık-veter oranının akış yapısı üzerindeki etkisinin oldukça önemli olduğunu göstermektedir. Düşük t / C oranı% 4.75 olan kanat, yüksek t / C oranına sahip kanatlara kıyasla belirgin bir şekilde daha yüksek atak açısında belirgin yüzey ayrımıyla karşılaşır. Sonuçlar delta kanatlarla ilgili daha önce yapılan çalışmalarda bildirilen tutarsızlıkların bazılarını açıklayabilir. Ek olarak, kanadın rüzgâr tarafından ayrılan kesme tabakasının kalınlığının kanat kalınlığı ile doğrudan ilişkili olduğu gözlemlenmiştir. Sonuç olarak, düşük ok açılı delta kanat üzerindeki akış yapısı t / C oranından oldukça etkilenir ve bu da kanat kalınlığının potansiyel bir akış kontrol parametresi olarak olası kullanımını gösterebilir.

Anahtar Kelimeler: Delta kanat, düşük ok açısı, üç boyutlu yüzey ayrılması, kanat kalınlığı, kalınlık-veter oranı

To my parents

ACKNOWLEDGMENTS

I would like to express my sincere gratitude to my thesis supervisor, Dr. Mehmet Metin Yavuz, for his guidance, support and irreplacable supervision throughout these years.

From first moment up to last moment of this thesis study, my colleagues Cenk Çetin and Gizem Şencan have always been helpful and I cannot express my gratitude to them in a couple of sentences. I wish success will always be with you in your life.

Alper Çelik, the most enthusiastic colleague on academic areas, has been a pioneer in many challenges of academic life and a good example to follow. It was a great pleasure to work and have fun with him.

I would like to thank my friends, Gökay Günacar, Emrah Güllü, Mohammed Reza Zharfa and Burcu Karagöz for their help in Fluid Mechanics Lab and friendship. Experimenting is a team work and I was lucky enough to have them around.

My dear friend Mert Erk has always been giving moral support and try to courage working hard on some scientific topics.

The technical assistance of Mr. Rahmi Ercan and Mr. Mehmet Özçiftçi are gratefully acknowledged.

TABLE OF CONTENTS

LIST OF FIGURES

FIGURES

LIST OF TABLES

TABLES

NOMENCLATURE

Greek Symbols

Λ	Sweep angle
α	Angle of attack
Ψ	Streamfunction
ρ	Fluid density
ν	Kinematic viscosity of air

Latin Symbols

C	Chord length
S	Spanwise distance at x/C=0.44
Re	Reynolds number based on chord length
U	Free stream velocity
V	Velocity vector
u	Streamwise velocity
w	Vertical velocity
ω	Vorticity
x	Chordwise distance from wing apex
y	Spanwise distance from wing root chord
Δt	Separation time between two pulses for PIV
Δ/C	Effective grid size
t/C	Thickness-to-chord ratio
z/C	Vertical-distance-to-chord ratio for PIV laser alignment
p	Surface pressure
$\bar{p}$	Average pressure
p_∞	Static pressure of the flow
p_{dyn}	Dynamic pressure of the flow

C_p	Dimensionless pressure coefficient
t	Thickness of the wing;
N	Number of samples in a measurement
PIV	Particle Image Velocimetry
ω_i	Uncertainty estimate of a variable i
u_i	Relative uncertainty estimate

CHAPTER 1

INTRODUCTION

An increasing interest on flow control of delta wings has been observed due to their common usage as simplified planforms of Unmanned Combat Air Vehicles, Micro Air Vehicles and Unmanned Air Vehicles. As a result, researchers focus on the improvement of aerodynamic performance of low swept (non-slender) delta wings [1]. During steady flight conditions or under defined maneuvers, complex flow structures appear over these vehicles, which must be well understood to optimize the flight performances [2], [3].

Classification of delta wings is based on the sweep angles as, non-slender (with sweep angles between 35^o and 55^o) and slender (with sweep angles greater than 55^o). Aerodynamicists have extensively studied unsteady flow structure over slender delta wings along with the effects of Reynolds number and angle of attack. On the contrary, studies on controlling the flow structure over non-slender delta wings are quite limited.

The flow over delta wing can be described as curved free shear layer resulted by flow separation from the windward side of the leading edges, which in turn, causes leading edge vortices (LEVs) that the flow structure has especially at a moderate incidences as seen in Figure 1.1 [3]. Formation of these vortices usually depends on the sweep angle, Reynolds number and the angle of attack. Moreover, the primary vortex interact with the boundary layer which develops at the inboard of the suction side of the wing and as a consequence of this interaction, with respect to primary vortices, secondary vortex arises rotating in opposite direction [1], [4].

As angle of attack increases, the delta wings experience different forms of instabilities including shear layer instability, vortex breakdown, vortex shedding,

vortex wandering and helical mode instability [1]. Breitsamter [4] stated that vortex breakdown arises at higher angles of attack by stagnation of the sudden expansion of the core and the jet-like axial core flow. In Gursul's study [5], formation of the breakdown and the movement are driven by two parameters: pressure gradient and swirl level. In Figure 1.2 [4], the flow structure over a delta wing can be seen with the schematic illustration of vortex breakdown.

Besides above instabilities, recent studies have introduced the concept of strong reattachment of the flow which arises after separation from the leading edge and attaches to the wing surface [5]. The reattachment line is through the inboard of the vortex core slender delta wings and exists only at low incidences. On the other hand, for non-slender delta wings, the separated shear layer reattaches to the wing surface by forming a vortex bound which has probability of occurrence even after the breakdown [3]. Figure 1.3 represents the schematic view of the cross flow pattern for slender and non-slender delta wings to indicate the concept of reattachment on the wing surface.

At sufficiently high angle attack, the vortex breakdown location moves toward to the vicinity of the wing apex and the stall condition might be experienced when the breakdown takes place at the wing apex [4]. For non-slender delta wings, the primary attachment takes place through the outboard of the wing surface, even after the breakdown reaches to the vicinity of the apex. This attachment line is directly related with the angle of attack such that an increase in the attack angle leads the movement of the attachment line toward to the inboard plane. Further increase in the angle of attack leads the elimination of the flow reattachment along with the coalescence of the vortex bounds from sides of the wings together with the stall [1].

All these flow instabilities have been extensively investigated for long years to optimize the flight performances. In these investigations, researchers have mostly studied on basic parameters such as Reynolds number, angle of attack and sweep angle. Although the effect of thickness-to-chord ratio on aerodynamic performance of delta wings have been investigated in some studies in literature [6]–[19], these investigations mainly focus on moderate and high swept delta wings without

characterizing the global flow field. As a result, t/C ratio studies have not drawn as much attention as the studies of Reynolds number, angle of attack and sweep angle.

1.1 Motivation of the Study

The flow over Micro air vehicles (MAV), Unmanned Air Vehicles (UAV) and Unmanned Combat Air Vehicles (UCAV) can be represented by nonslender delta wing planforms. During the steady flight and defined maneuvers, complex flow patterns exist over their wings which must be well understood and characterized to optimize the flight performances especially by eliminating three-dimensional surface separation/stall, and enhance reattachment.

The effect of thickness-to-chord (t/C) ratio has been studied experimentally and analytically with particular interest in aerodynamic performance of high and moderate swept delta wings [6]–[19]. These studies have mainly reported the thickness effect on aerodynamic forces where global flow field has not been quantified. In addition, considering the low swept wings, no study, focusing on t/C ratio, has been conducted. Therefore, the effect of t/C ratio on characterization of global flow field over low swept delta wings needs to be investigated and quantified for aforementioned optimization of flight performances.

1.2 Aim of the Study

The current study aims to characterize the effect of t/C ratio on flow structure of a delta wing with sweep angle of 35 degree. For this purpose, four delta wing models have been designed and manufactured with t/C ratio varying from 4.75 % to 19 %. Experiments were conducted in a low speed wind tunnel using laser-illuminated smoke visualization, surface pressure measurement, and near surface and cross flow particle image velocimetry (PIV). Reynolds numbers of Re=10,000 and 35,000 for the angles of attack varying from 4 to 10 degrees were utilized to cover wide ranges of flow regimes including three dimensional surface separation and leading edge vortex.

1.3 Structure of the Thesis

In this thesis, five main chapters are provided. Chapter 1 includes the introductory information about the flow over delta wings and the aim of the study as well as the motivation.

Chapter 2 involves detailed information about flow physics of delta wings along with previously conducted studies in literature about these and especially effect of the thickness-to-chord ratio which is the main topic of the present study.

Chapter 3 summarizes the measurement techniques used in the present study. In addition, details of the experimental set-up and matrix are provided.

The results of the effect of t/C ratio on flow structure of a low swept delta wing are summarized and discussed in Chapter 4. Laser-illuminated flow visualizations and pressure measurements results are presented. Then, PIV results along with laser-illuminated flow visualization and pressure measurement for selected cases are discussed for global characterization.

Finally, the conclusions of the present study along with the recommendations for future work are presented in Chapter 5.

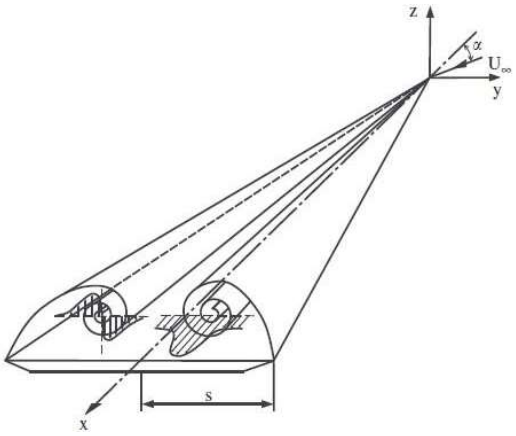

Figure 1.1 Schematic representation of shear layer and leading edge vortices over a delta wing [3].

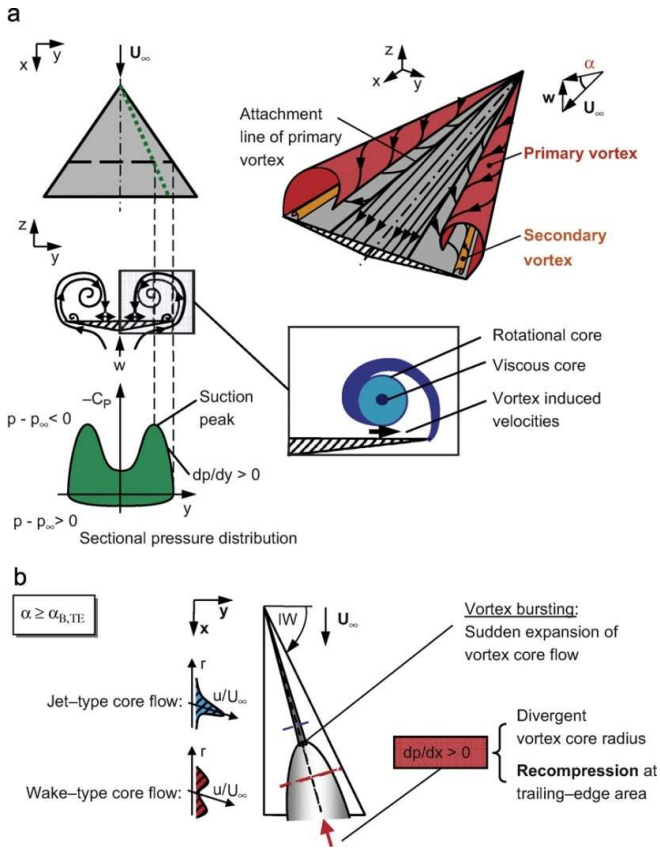

Figure 1.2 Delta wing vortex formation: (a) main delta wing flow features and (b) vortex bursting characteristics [4].

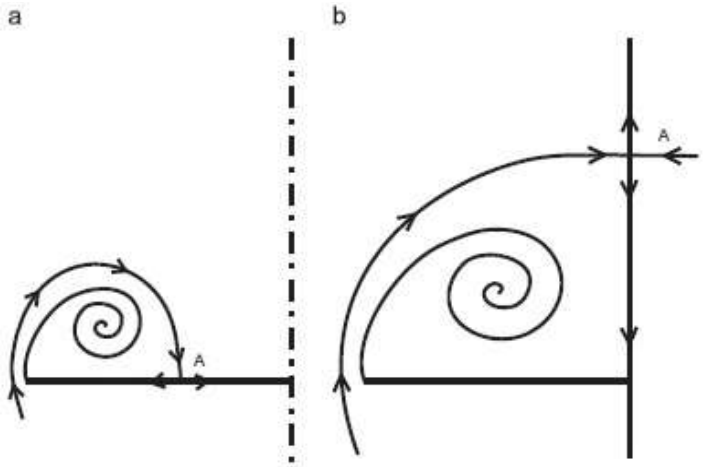

Figure 1.3 Schematic streamline patterns (a) for reattachment over nonslender wings and (b) with no reattachment on wing surface on slender [3].

CHAPTER 2

LITERATURE SURVEY

In this chapter, detailed information about flow physics of delta wings and the effect of the thickness-to-chord ratio along with previously conducted studies in literature about these are given under the topics: flow past delta wings, separated shear layers and instabilities, vortex breakdown, flow reattachment & stall and effect of thickness-to-chord ratio.

2.1 Flow Past Delta Wings

There have been many studies about the flow structure over delta wings which have revealed major differences between slender and non-slender delta wings. In this part, flow characteristics of non-slender and slender delta wings will be presented and compared.

The flow over a delta wing is governed by two counter-rotating vortices evolved from the leading edges. After separating from the leading edge, the free stream turns into curved free shear layers on delta wing surface [3]. On the suction side, lower pressure and higher velocity profiles are observed in comparison with the free stream conditions as a result of energy conservation of the flow over the wing. These differences lead generation of lift force on the planform. In the early history of delta wings, detailed research was made by Werle [20], Earnshaw and Lawford [21], Bird [22], Polhamus [23] and Erickson [24]. In these studies, vortex flows were studied and vortex breakdown arising with increasing angle of attack was reported. Furthermore, vortex breakdown search also were pursued by scientists including Benjamin [25], [26], Sarpkaya [27]–[29], Wedemayer [30] and Escuider [31]. The discrete vortices resulted by flow separation over the slender wings were

investigated by Gad-el-Hak and Blackwelder [32]. In another study, time averaged axial velocity component of the vortex core was reported to be as four or five times of the upstream velocity for slender delta wings by Gursul [5]. For non-slender delta wings, distance between vortices which are formed at low angle of attack to wing surface was observed less than the distance between vortices of the slender wings and wing surface by Ol and Gharib [33]. This characteristic was linked with significant differences in the flow structure such as boundary layer interaction, reattachment and additional vortex formations. As a result of separation of the secondary flow from the wing surface, primary vortex splits and dual vortex structure is seen for non-slender delta wings in the main core at low angles of attack. Gordnier and Visbal [34] first pointed out this dual vortex formation computationally and its existence was confirmed Taylor et al. [35] with Particle Image Velocimetry (PIV) measurements and also by Yanıktepe and Rockwell [36]. Jin-Jun and Wang [37] performed a broad experimental search in favor of improving dual vortex structure. At the end, it was concluded that the range of the angle of attack having dual vortex got narrow along with increase in wing sweep angle. Figure 2.1 represents the sketch of dual vortex structure [37].

Gursul [38], Gordnier and Visbal [39], Yanıktepe and Rockwell [36] and Ashley et al. [40] started to study on the unsteady nature of the aforementioned flow structures over slender delta wings. Menke et al. [41], Gursul and Xie [42], and Nelson and Pelletier [43] went on contribution with their detailed investigation and review. Taylor and Gursul [44] performed Particle Image Velocimetry (PIV) and Laser Doppler Anemometer (LDA) measurements to understand the buffeting response and unsteady vortex flow. Yavuz et al. [45] pinpointed the near surface flow patterns by applying PIV for a delta wing with sweep angle of $\Lambda=38.7^{o}$. Öztürk [46] carried out LDA and surface pressure measurements for a non-slender delta wing to clarify three dimensional surface separation and its unsteady nature. Zharfa et al. [47] conducted laser-illuminated flow visualization, pressure measurements and Laser Doppler Anemometry to examine the flow structure over a $\Lambda=35^{o}$ delta wing.

2.1.1 Separated Shear Layers and Instabilities

Viscous flow theory indicates that separation occurs when the flow interacting with a body experiences an adverse pressure gradient and boundary layer theory becomes invalid after then. The separation always takes place on the sharp-edge delta wings. Earnshaw [48] told that rotational core, viscous subcore and free shear layer are three different regions of the vortex resulted by the separation and these regions are illustrated in Figure 2.2 [49]. In addition, Özgören et al. [49] highlighted the unsteady flow nature of a slender delta wing, which agrees with the instabilities concluded by Riley and Lowson [50].

Gordnier and Visbal [34] stated that shear layer instability is resulted from sudden expansion of the secondary flow and this is caused by vortex wandering which arises from the interaction of surface boundary layers with primary vortex. Figure 2.3 represents the instantaneous vortical flow structure over 50^{o} swept delta wing [34].

2.1.2 Vortex Breakdown

As a result of increasing angles of attack, leading-edge vortices experience vortex breakdown which is a sudden expansion of vortices and the basic definition can be made as a sudden change in vortical structure. Expansion of the vortical core up to the boundaries of the flow field results in a jet-like axial flow which leads an obvious deceleration [51]. This result also means change of the axial flow upstream to wave like flow with a remarkable decrease in velocity [3]. After the breakdown, aforementioned decrease in velocity results in an increase on the suction side. At the end, a dramatic drop in both momentum and lift coefficient takes place. In other words, aerodynamic capabilities are lost up to stall conditions. Previous study done shows that the vortex breakdown has seven different kinds [52]. Bubble and spiral vortex breakdowns are mostly observed over delta wings. The latter was generally observed in the cases of slender delta wings [20]. Gursul et al. [1] used flow visualization technique to observe the vortex by providing smoke or dye to the flow

field. In another study, Lambourne and Bryer [53] clarified the phenomenon over a slender delta wing with a sweep angle of $\Lambda=65^{o}$, in Figure 2.4. Erickson [24] also concluded that observations of the breakdown location in wind tunnel were in line with real flight observations.

Contrary to slender wings, non-slender delta wings have difference on the topic of vortex breakdown. Due to their geometry, they are prone to display more conical shape of the breakdown where no swirling or reversed axial flow in the vortical core has been observed as it is for slender ones [36], [44]. In his early search, Lowson [54] demonstrated that the vortex breakdown location is reported to fluctuate along the streamwise direction over a stationary slender delta wing. Furthermore, Ol et al. [33] and Taylor et al. [35] showed identical fluctuations over almost half of the chord for non-slender delta wings whereas this range was 10 % of chord for slender delta wings [54]. Gursul [5] and Yavuz [55] stated that aforementioned fluctuations may cause wing buffeting which has significant role for stability and control issues.

2.1.3 Flow Reattachment & Stall

Flow reattachment is another characteristics of non-slender delta wings [1]. Shear layers that separated from leading edges simply attaches to the wing surface. For the slender delta wings, this phenomenon does not occur beyond the low angles of attack [3] where its control is difficult. For non-slender wings, reattachment is more likely to be seen, especially over a wide range of incidences. Honkan and Andreopulos [56] experimentally studied with a moderate swept wing to characterize flow reattachment over flow structure by using spatio-temporal measurement techniques. In the end, they concluded that the secondary vortices and reattachment area are linked to high percentage of turbulence intensity. Taylor and Gursul [44] made detailed experimental search for a 50^{o} swept delta wing and observed the movement of the primary reattachment line to the wing centerline as the angle of attack increases, and complete stall when it reaches the centerline,

meaning that the flow cannot reattach to the wing surface. The reattachment progress over a delta wing is illustrated in Figure 2.5 [44].

Peake and Tobak [57] associated reattachment and three dimensional surface separation by applying the fundamental laws of flow topology aiming to establish flow basics with singular points concept: saddles, nodes and spiral nodes. Gursul et al. [3] made comparisons on the characteristics of reattachment and vortex breakdown as a function of both sweep angle and incidence by collecting data from several studies investigating the stall onsets which is given in Figure 2.6. For non-slender delta wings, the reattachment can be relocated into the post stall region by applying flow control techniques and they are expected to provide improvement in lift which means postponing of stall condition.

Ericsson [58] delved into the effect of different leading edge cross-section on delta wing which may be accepted as gathering of different leading edge shape and different wing planform thickness. The effect of different wing planform thickness means that the only parameter in the study is changing thickness, which is studying on a bunch of identical delta wings except their thickness-to-chord ratios. Since this topic is the topic of the main study, it will be explained under next sub-title.

2.2 Effect of Thickness-To-Chord Ratio

In the history of delta wings, the effect of thickness-to-chord ratio has been examined in few ways. Some scientists have searched that whether changing the thickness affects the flow or not, some of them have considered thickness issue with multiple cases with leading edge [58]. At the beginning of delta wing history, Polhamus [23] concluded that modifications on wing geometry resulted in unfavorable effects on flow such as absence of ability to predict the spread and origin of the separated flow, stability, performance and control problems. He stated that aforementioned effects became apparent along with an increase in wing sweep angles and a decrease in the thickness which makes thickness issue important. In another study, Délery [59] pointed out the significance of sharp leading edge usage

on delta wings and he subsequently commented on Werle [60] 's experiment on a thick and round leading edge delta wing. He proposed to increase thickness and have sharp leading edge for improvement over the flow topology of Werle [60] 's experiment. The thickness effect was also studied with analytical methods by Ruo & Theisen [61]. They stated that thickness effect was used to be neglected for unsteady transonic flow theoretical work. However, the fact that oscillatory transonic aeroelastic instabilities of lifting surfaces often occur at frequencies below the range of validity of the transonic linearized theory made an inevitable necessity to introduce the effect of finite thickness. For this purpose, Kacprzynski et all [6] were on charge and they explained the significance of thickness effect on the lift, aerodynamic center, and flutter speed of a delta wing for supersonic flow and for transonic flow range on the aerodynamic forces on a finite wing. They used the thickness effect through the use of the local Mach number of the wing at its mean position in the unsteady, small perturbation equation.

Parker [7] collected data from researches of Peckham [8], Berndt [9] and Garner & Lehrian [10]. With the data, he built Figure 2.7 below which presents positions of the center of pressure resulted from balance measurements and theory for a unit aspect ratio wing. The results show that the center of pressure seems to move aft as thickness increases for sharp-edged wings. He also stated that in Berndt [9]'s experiments, sharp edged wings showed a reduction in C_N values when thickness of wings is increased. Peckham [8] concluded that thickness affect as a localizer of the leading-edge separation at low incidences by leaving the flow external to the boundary layer relatively undisturbed. On the other hand, this effect represents that the coiled vortex sheets do not develop as rapidly for thick wings as they do for flat plate wings. Peckham [8] also concluded that increasing thickness is seen to move the vortex system outboard.

Thompson [11] made comparisons between same experimentations in literature. He observed a 25 % difference in vortex breakdown location for a fixed angle of attack especially between two studies on same configuration. He linked these by making

a generalization that the cause for difference may be resulted from leading edge geometry, thickness-to-chord ratio, measurement technique/researcher defined breakdown point, blockage, wing support interference, or the direction of quasi-steady motion (increasing or decreasing angle of attack). Moreover, he studied on flat plate delta wings having 70^o sweep angles and thickness-to-chord ratios varying from 3.1 to 4.6. He concluded that change of thickness (from a thicker to a thinner wing) makes the vortex breakdown location move closer to aft for a given angle of attack. At the end; unfortunately, his data about effect of thickness-to-chord ratio was not consistent with other published data in literature. Lowson and Ponton [12] performed experimental and theoretical researches for the observation of asymmetric flows on conical bodies including delta wings. They used two delta wings having sweep angles as 70° and 80° and bevel angles as 70°. The tests covered a range of Re varying from 20000 to 3000000. The experiments were conducted at incidence range from 0^o to 90^o. Experimental results on two slender delta wings concluded that there would be no asymmetric vortex flow on the two wings before the onset of vortex breakdown. They concluded that thickness effect was observed on the onset angle of attack for asymmetric vortex flow. In other words, for a thinner delta wings, vortices would never experience asymmetry when the thickness kept small.

Witcofski and Marcum Jr. [14] made experiments to determine the effects of thickness and sweep angle on the longitudinal aerodynamic characteristics of basic delta wings. Delta wings had sweep angles moderate to high as 45^o, 60°, 70°, 80°, 85^o, and 90° and thickness-to-chord ratio range was between 0 and 0.3. Reynolds number based on wing length varied from $1.4x10^6$ to $6.6x10^6$ and the angle-of-attack range was approximately from 0^o to 30°. In Figure 2.8, maximum lift-drag ratios are presented as a function of t/C ratio for each sweep angle mentioned above and it has an important characteristic such that $(L/D)_{max}$ exhibits a nearly linear decay as thickness ratio is increased logarithmically. Moreover, optimum sweep angle - $(L/D)_{max}$ relation for each thickness-to-chord ratio is represented in Figure

2.9 and results demonstrate that the optimum sweep angle for maximum lift-drag ratio decreases from an angle slightly larger than 80° to 70° or less for the highest thickness-to-chord ratio as t/C ratio increases. In Figure 2.10, the slopes of the normal-force curves and lift curves at zero angle of attack as a function of t/C ratio is presented for each sweep angle and it can be concluded that as thickness-to-chord ratio increases, the slopes of the normal force and lift force at an angle of attack 0^o increase almost linearly. Figure 2.11 is presented by groups of particular sweep angles and each group has its own thickness-to-chord ratios where the relation between the center of pressure and angle of attack of each case is shown. The results state that the center of pressure moves forward from the two-thirds-root-chord point as thickness-to-chord ratio increases. Furthermore; in Figure 2.12, there are groups of particular thickness-to-chord ratios and each group has its own different sweep angles showing the relation between the center of pressure and angle of attack of each case. The results indicate that as sweep angle decreases, the center of pressure of the wings having higher thickness-to-chord ratios is seen to move rearward.

Lowson and Riley [15] investigated why the vortex breakdown location on delta wings having similar sweep angle differs. Many studies seemed to have identical results in which the wing leading edge was kept sharp. Nonetheless, he realized differences in results of details of similar model geometry in slender wings. The main reason for differences was thickness-to-chord ratio. They stated that a decrease in wing thickness will tend to move the location of the vortex breakdown aft and the effect will be observed about 5^o-7^o variation in angle of attack for a given vortex breakdown position. Shih & Ding [62] contributed to this debate with their search on the effect of using a trailing-edge jet to control the leading-edge vortices. They realized significant disagreements on their data when compared to previous data on same design. To be more exact, they repeated experiments using a thinner wing with a thickness-to-chord ratio 4.2 % and presented the relation between vortex breakdown location and static angle of attack of their data with previous data from Wentz & Kohliman [13] and Miau et all [16] in Figure 2.13. The results

represent that the disagreements primarily were caused by the former thick wing with a t/C=20 %. Wang and Lu [17] contributed the debate by studying both the effect of leading-edge bevel angle and thickness-to-chord ratio on delta wings with a sweep angle of 50. The tests were conducted on delta wings with t/C ratios as 2 %, 6.7 % and 10 %. Among them, the delta wing with t/C= 0.02 was 30°, 45° and 60° windward and leeward beveled whereas delta wings with t/C=0.067 and 0.01 were 15°, 30°, 45° and 60° windward and leeward beveled. At the end, the thin delta wing exhibits a better performance than thicker delta wings due to higher maximum value of C_L/C_D.

Nakajima et al. [18] made experiments on a thick and round leading edge delta wing and compared with thin one. Except flow pattern, there were similarities between thick wing and thin wing. A thick delta wing and three thin delta wings were used in experiments for comparison. Models had a 45-degree sweep angle, 220 mm chord length and 440 mm span. Thick delta wing also had round leading edge and 13.6 % thickness ratio. On the contrary, thin delta wings had rectangular leading edge with a 3.41 % thickness-to-chord ratio. Reynolds number for smoke wire visualization was $0.5x10^5$, for tuft and oil visualization was $1.5x10^5$. Results were generally same for both different thickened delta wings but there were some differences. For instance, flow visualization told that, for thin delta wing, stall occurs at slightly lower angles of attack than thick delta wing. Pressure measurements also showed that leading edge vortex produces hill-like pressure distribution at an angle of attack of 15^o for thin delta wing, while it produces a knife-edge like pressure distribution at the same angle of attack for thick delta wing. In addition to that result; at 20^o angle of attack, because of strong suction force, it was concluded that the LEVs of the thin delta wing are stronger than LEVs of thick delta wing when they are fully developed. Kawazoe et al. [19] investigated experimentally the flow structure over a thick and round leading edge delta wing and made comparisons with a thin delta wing with small round leading edge. Both wings had 45^o sweep angle, 220 mm root-chord and 440 mm span. Thicker wing

had a thickness of 20 mm with a t/C ratio of 9.1 % and thinner one had a 9 mm with a value of t/C ratio 2.7 %. Reynolds number based on wing length was $2.2x10^5$ for all experiments. At the end, important differences and results were observed. In Figure 2.14, the lift coefficient C_L, and the drag coefficient C_D of both thick and thin delta wings as a function of angle of attack are presented. Measurements were done with three-component force balance. From these forces also, Figure 2.15 is plotted which shows the relation between the lift-drag ratio, L/D. L/D and coefficients usually exhibit similar behaviors except certain differences: C_D of the thick wing is slightly greater than the C_D of the thin one at small angles of attack. At higher angles of attack, C_L of thin wing seems to be 0.1 higher and as a main conclusion, it could be stated that the stall condition is observed at a more angle of attack value in the thick wing than the thin one. These values are more than 25^o for the thick wing and a value between 20^o and 25^o for thin wing and Kawazoe et al. [19] concluded that angles of attack at stall conditions are different due to the difference in LEV size: for thin delta wing, the vortex size develops wider than thick one. As a result of this fact, vortices coming from both leading edges collide quicker, i.e. at lower angle of attack for thin wing, which means stall condition.

In addition to basic experimental cases, the effect of thickness-to-chord ratio on delta wings was studied on further detailed applications. Golparvar, Irani and Mousavi Sani [63] performed experiments on nonlinear and linear aeroelastic behavior of a cropped delta wing. They made experiments and analytical investigations for the t/C ratio parameter on both instability boundary and flutter speed of the wing. The effect of t/C ratio is given in Figure 2.16. On the left side in Figure 2.16; as the wing thickness increases, the dimensionless flutter speed of the model increases. For each thickness versus $\eta_{s,}$ the rate of change in flutter speed is observed to be the same. On right side in Figure 2.16, the dimensionless frequency of flutter decreases up to the turning point and then increase along with an increase in thickness of the wing. In the end, experimental aeroelastic investigations of the

wing/store configuration revealed that its the flutter speed will be increased as thickness of plate is increased.

Saltzman and Ayers [64] made comparison on two wings of two airplanes: XF-92A and YF-102. Both airplanes had 60^o delta wings and 60^o delta tails. The XF-92A had a t/C ratio of 6.5% and the YF-102 a t/C ratio of 4%. Figure 2.17 represents the variation of the drag coefficient as a function of Mach number for each delta wing. It has two flight data for each wing and one wind-tunnel model for delta wing of YF-102 airplane. The drag divergence Mach number of the YF-102 configuration seems to be 0.03 higher than and the wave drag increment is about two-thirds of the value of XF-92A configuration which has a thicker wing. In another study, Tang, Henry and Dowell [65] stated that a constant plate thickness delta wing could show limit cycle oscillations (LCOs) of the order of the plate thickness and they constructed a delta wing model from a 0.079-cm-thick aluminum alloy sheet, besides 0.24-cm-thick plastic plate to check the effects of the plate thickness. In the end, the results were not in line for the plastic model, and there was a larger error between experiment and theory in the range of higher velocities both for the frequency and amplitude of the LCO. The main cause of this was reported as the initial plate curvature of thin aluminum model. McClain et al. [66] investigated experimentally free-to-roll delta wings. The wings had 50^o sweep angle, 200 mm chord. However; as aforementioned before, there were a second variable besides thicknesses of wings which was leading edge profile. There were six wings with a range of thickness-to-chord ratio 1.51 % to 10 % and leading edge profiles were sharp-edged single bevel, semi-circular, 2:1 ellipse, 4:1 ellipse, sharp-edged double bevel, and semi-circular profiles. In the conclusion part, it was told that the amplitude of the self-excited roll oscillations observed in a small range of angle of attack decreases as thickness-to-chord ratio decreases.

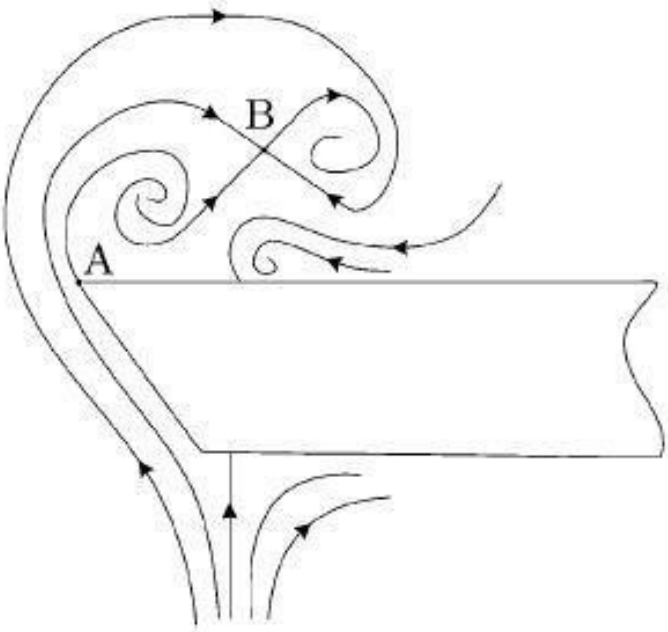

Figure 2.1 Sketch of dual vortex formation [37].

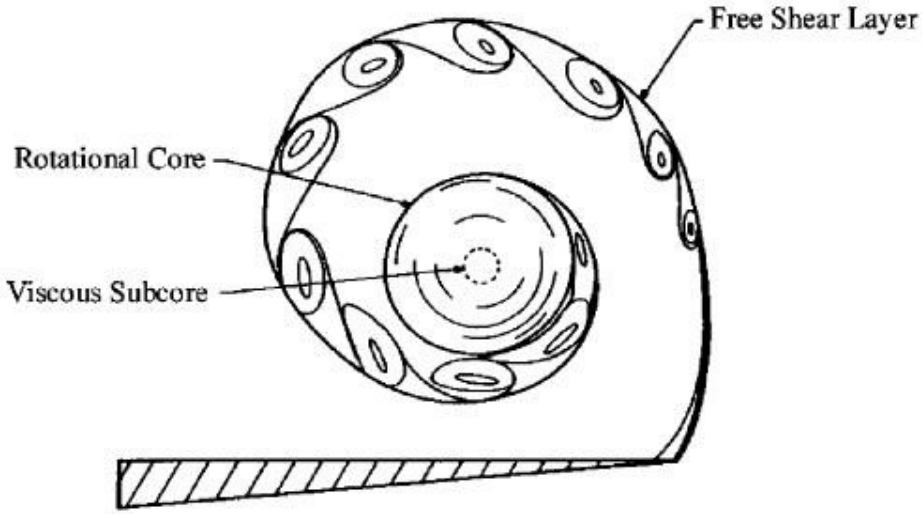

Figure 2.2 Illustration of free shear layer, rotational core and viscous subcore over a delta wing [49].

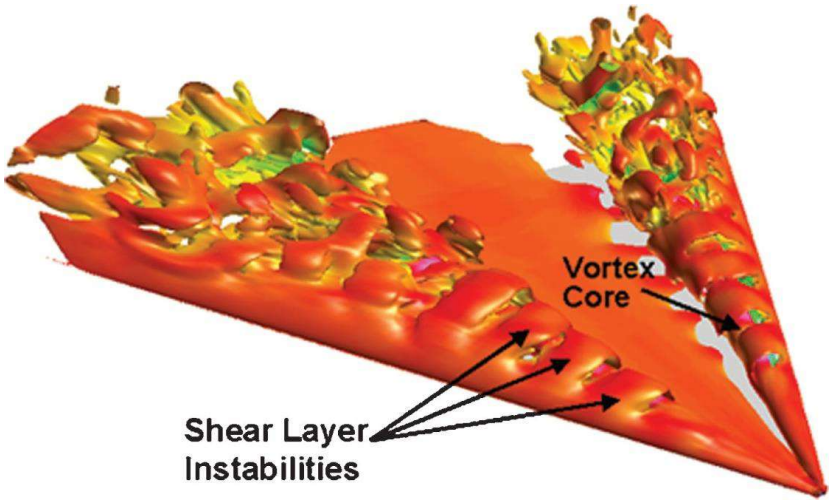

Figure 2.3 Instantaneous vortex structure over a delta wing [34].

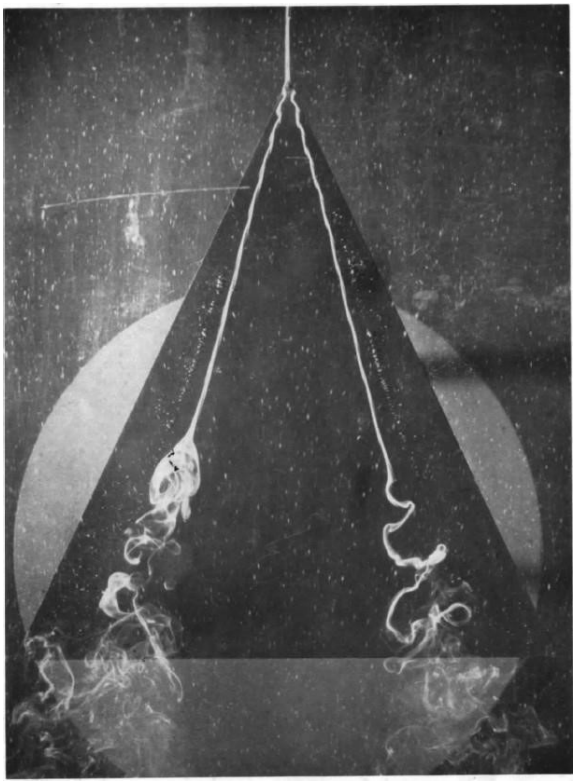

Figure 2.4 Vortex breakdown visualization [67].

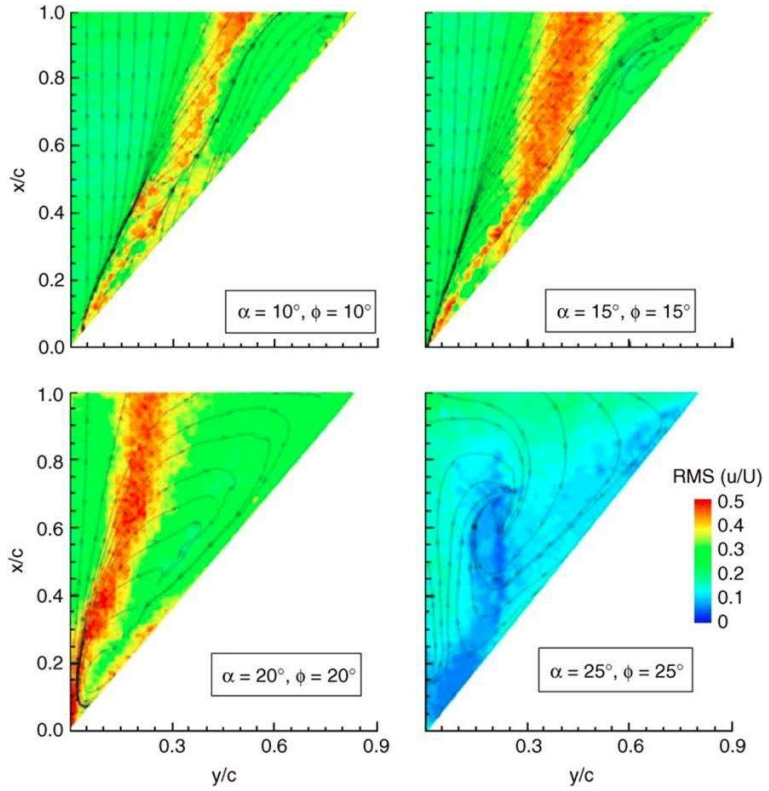

Figure 2.5 Magnitude of time-averaged velocity and streamline pattern near the wing surface in water-tunnel experiments breakdown visualization [44].

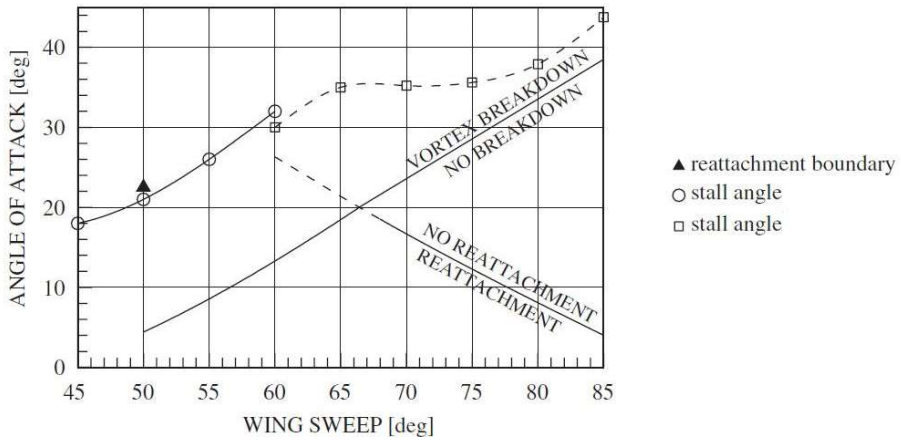

Figure 2.6 Boundaries of vortex breakdown and flow reattachment as a function of angle of attack and sweep angle [3].

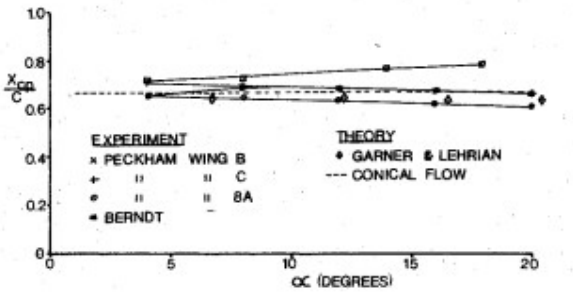

Figure 2.7 Position of center of pressure [7].

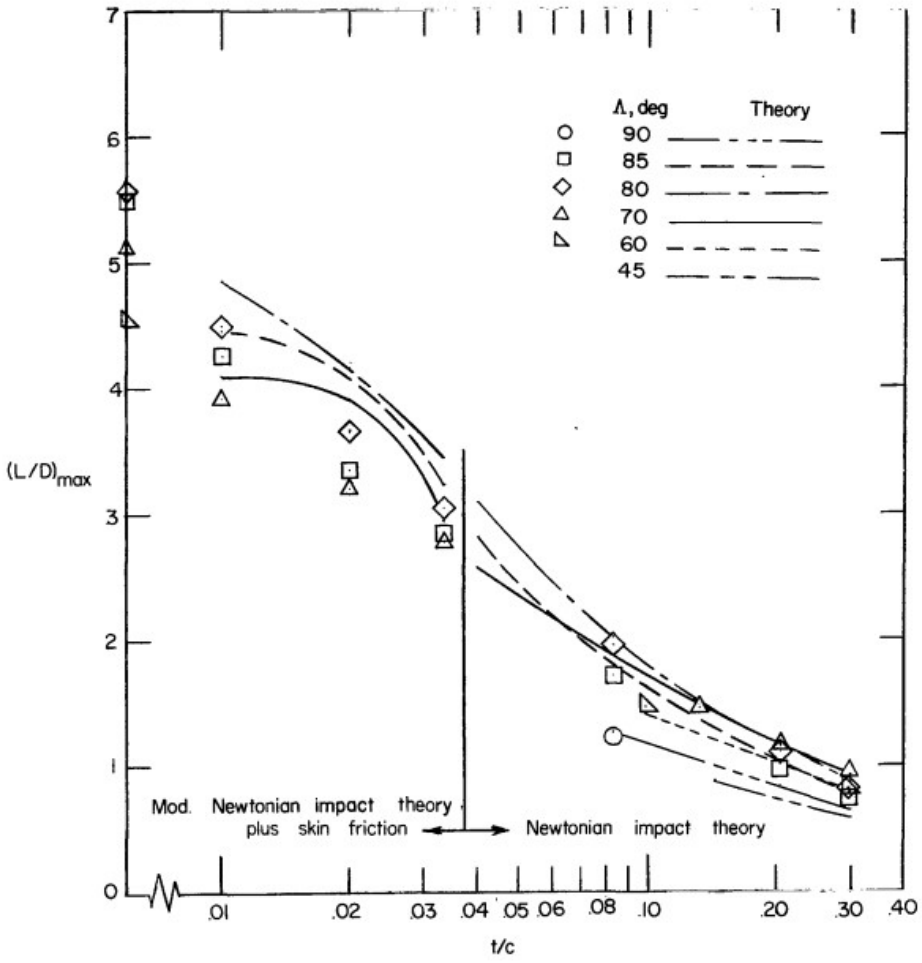

Figure 2.8 Maximum lift-drag ratio as a function of thickness-to-chord ratio [14].

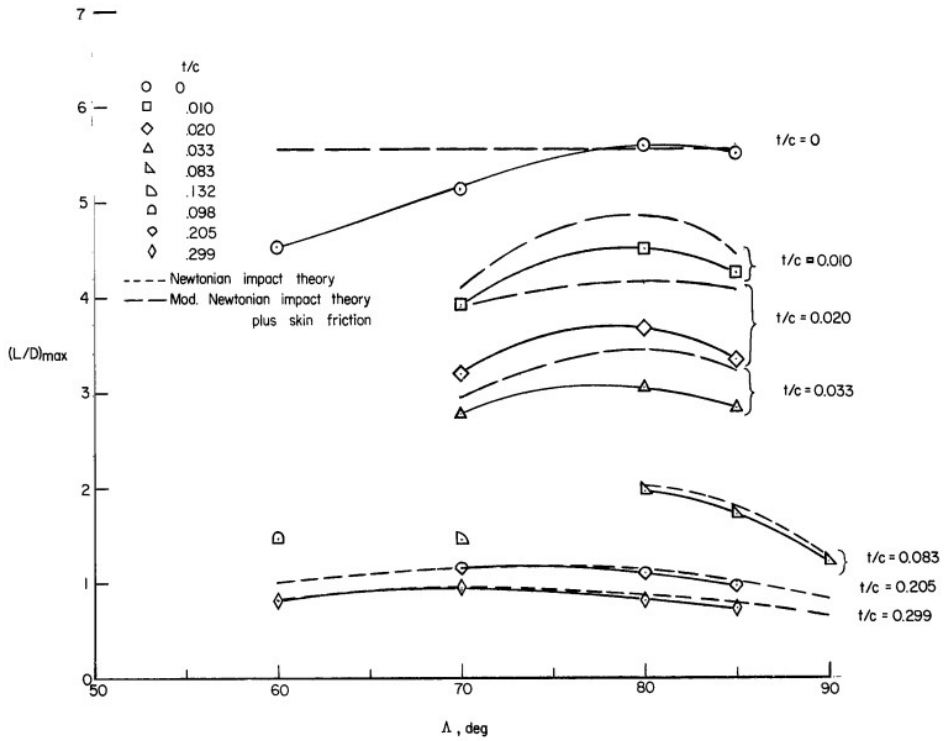

Figure 2.9 Variation of (L/D)max with sweep angle [14].

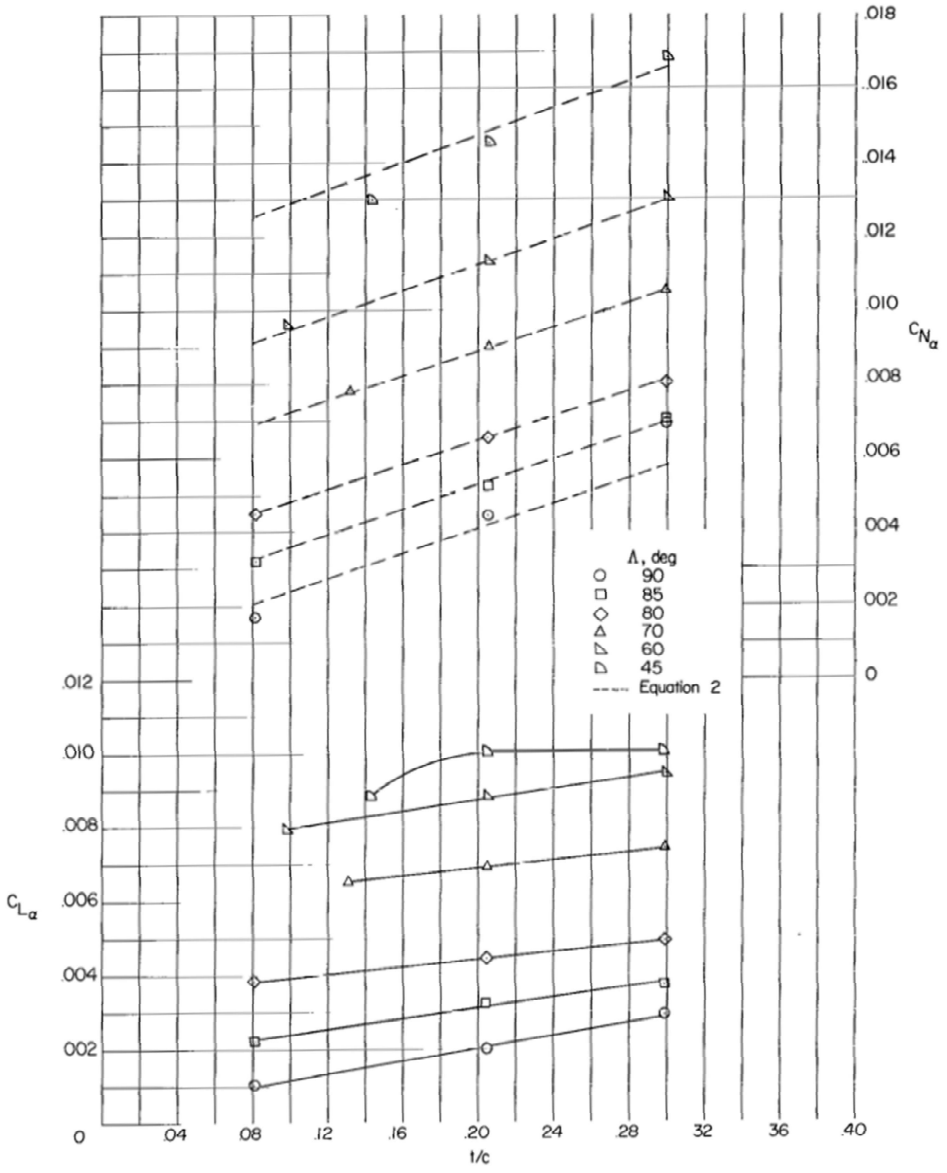

Figure 2.10 Slopes of normal-force curves and lift curves at zero angle of attack as a function of thickness-to-chord ratio [14].

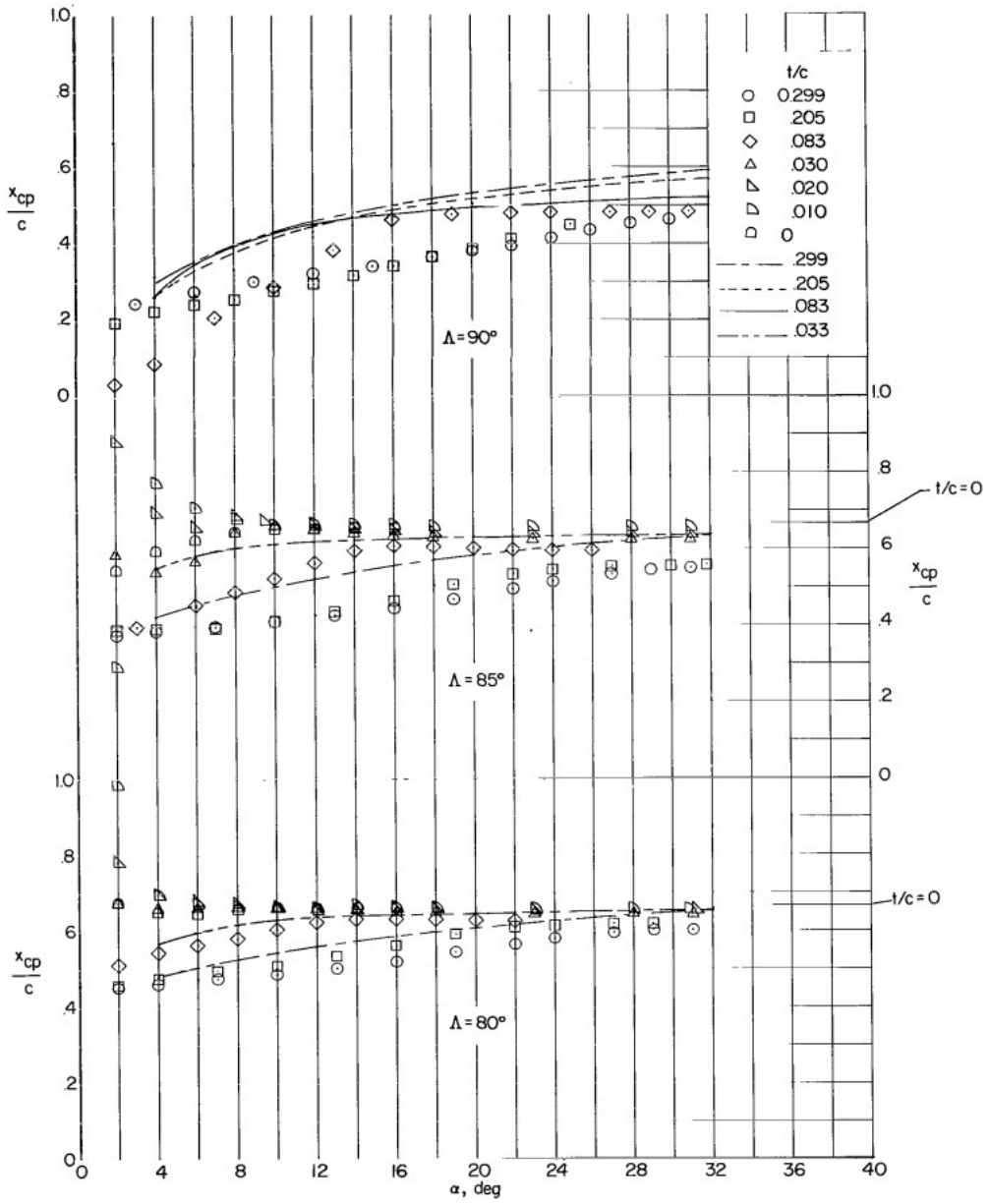

Figure 2.11 Variation of center of pressure with angle of attack [14].

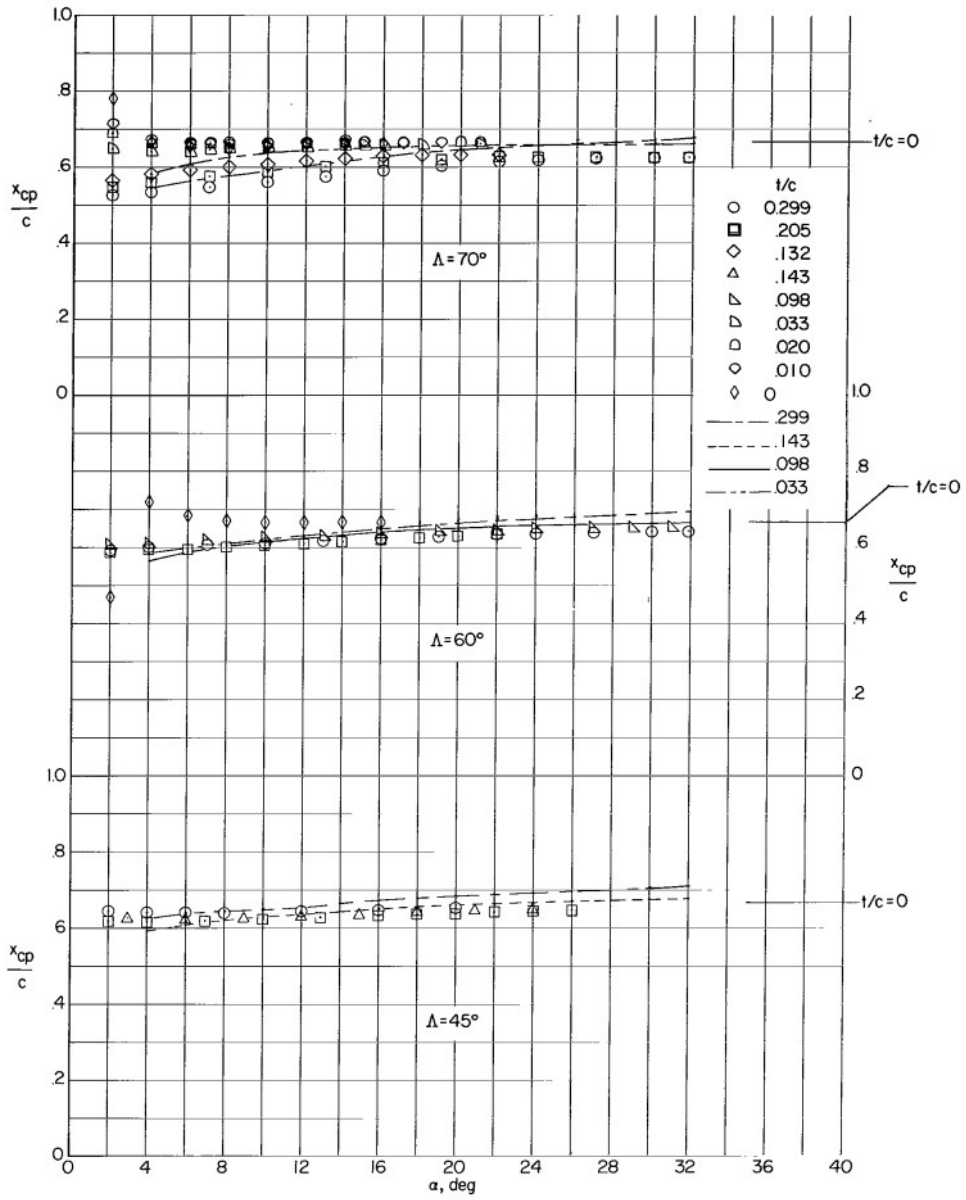

Figure 2.11 Concluded [14].

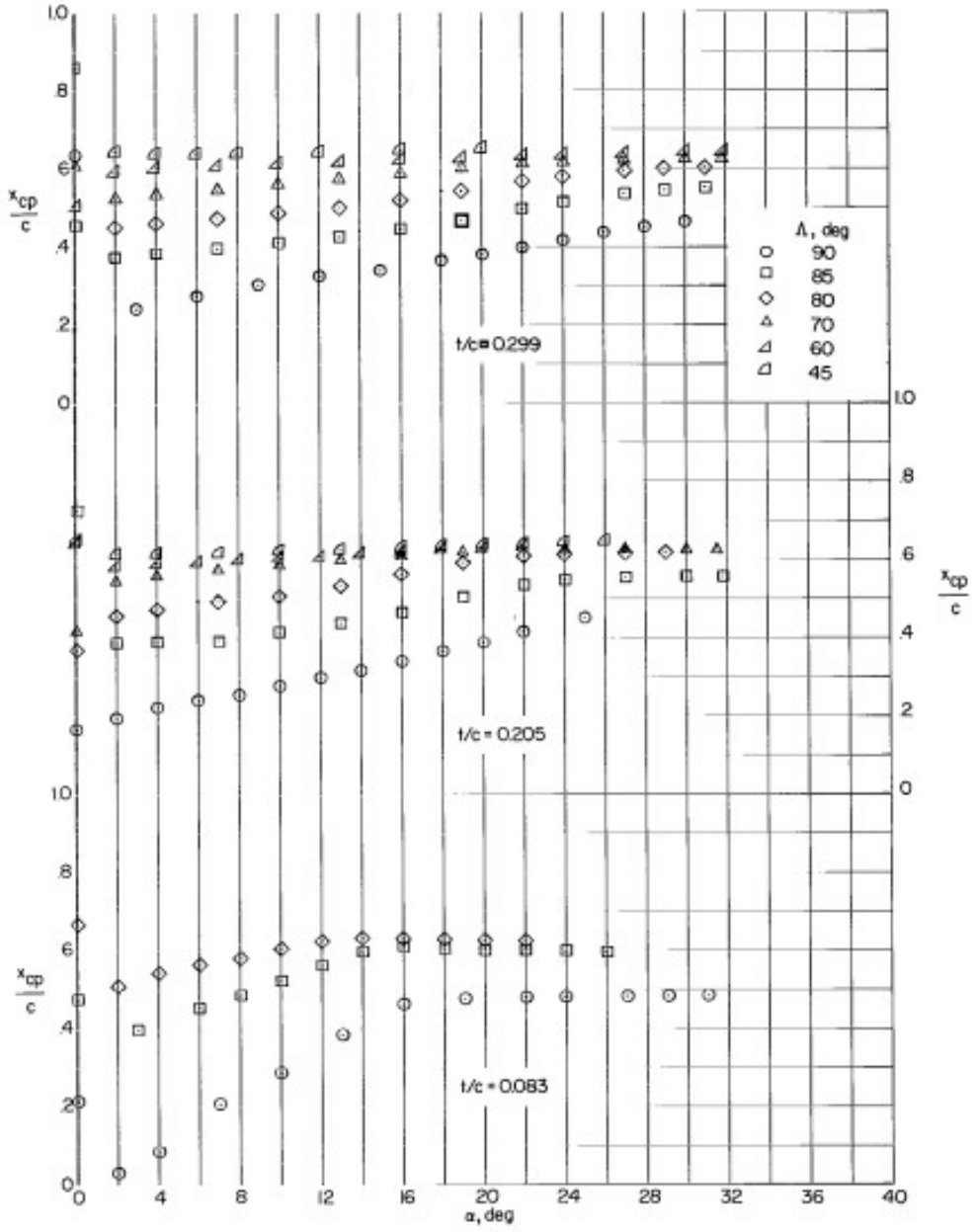

Figure 2.12 Variation of center of pressure with angle of attack [14]

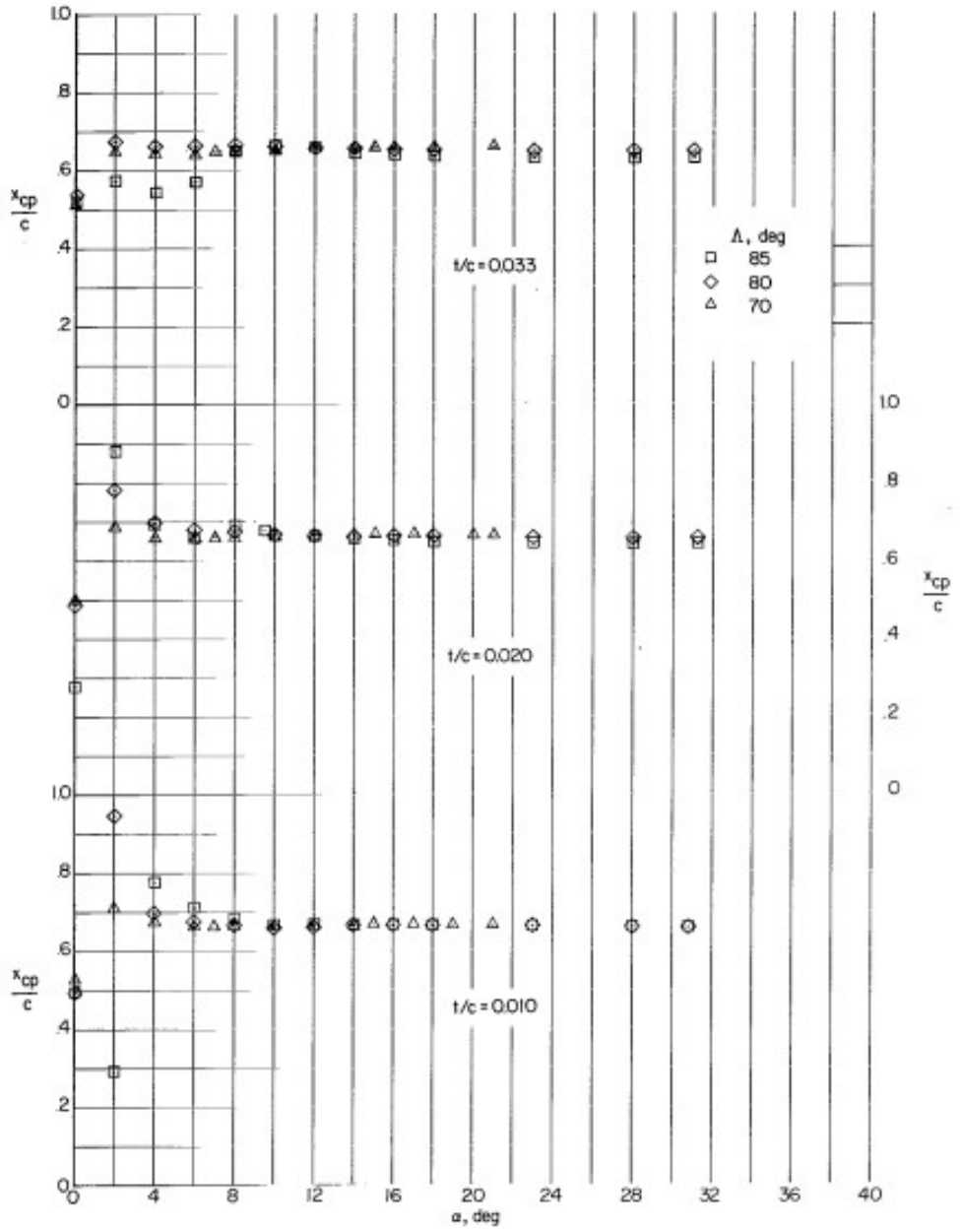

Figure 2.12 Concluded [14].

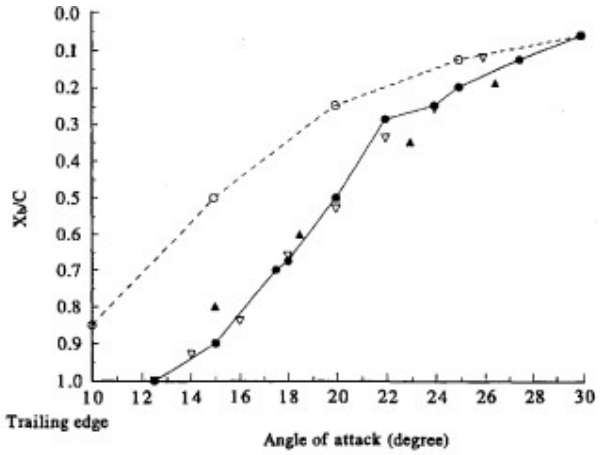

Figure 2.13 Comparison of vortex breakdown location: Δ, Wentz et all[13]; and ∇, Miau et all [16];◦, thick delta wing; •, thin delta wing [62].

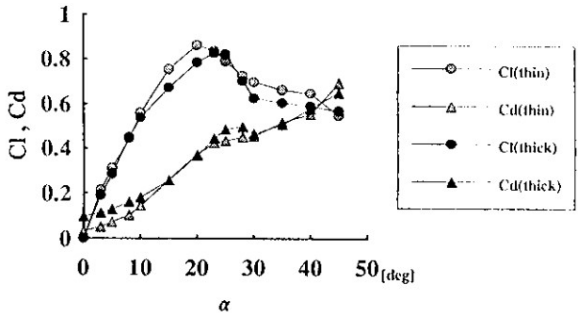

Figure 2.14 Lift and drag coefficients, C_l and C_d [19].

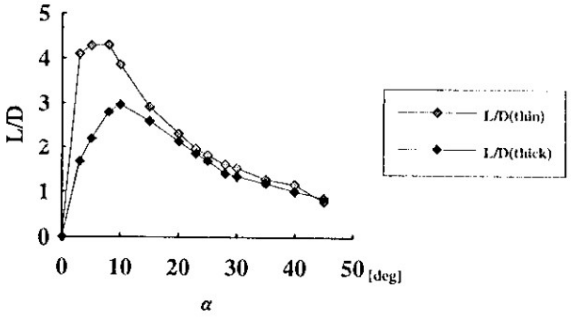

Figure 2.15 Lift-drag ratio with angle of attack [19]

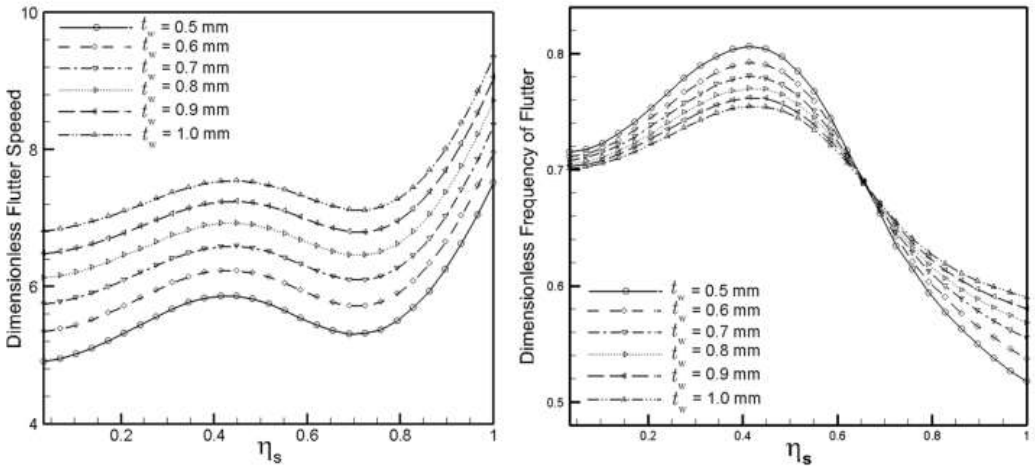

(a) (b)

Figure 2.16 Variation of dimensionless (a) flutter speed and (b) frequency versus dimensionless span location of store, for various values of the thickness of wing [63].

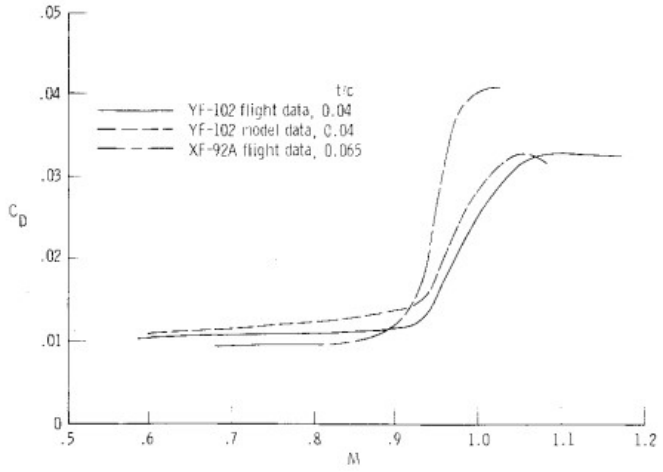

Figure 2.17 Effect of wing thickness-to-chord ratio on drag divergence mach number and the wave drag increment [64].

CHAPTER 3

EXPERIMENTAL SET-UP AND MEASUREMENT TECHNIQUES

3.1 Wind Tunnel

The experimental study were conducted in an open circuit, suction type and low-speed wind tunnel, shown in Figure 3.1, in the Mechanical Engineering Department at Middle East Technical University.

Air comes into the tunnel via two inlets. In order to enhance the uniformity of air and to eliminate the intrusion of any unfavorable materials to the test section, fine-mesh screens are placed at inlets. In addition, for the purpose of having low turbulence intensity and uniform flow in the test section, three fine grids and a honeycomb are mounted in the settling chamber. Before air enters into test section, contraction section causes a substantial increase in free stream velocity by reducing the area. The settling chamber and contraction section are 2700 and 2000 mm long, respectively. The contraction section has the contraction ratio of 8:1.

In order to measure velocity with laser-based techniques, optical access to flow field is required and provided via a fully transparent, Plexiglas test section. The test section dimensions are 510 mm height, 750 mm width and 2000 mm length. The top, bottom and sidewalls of test section are transparent to access to the inside for adjustment of experiments. The maximum achievable free stream velocity is 30 m/s. After air exits the test section, 7300-mm-long diffuser with a 3° cone angle decelerates the high-speed flow which results in static pressure recovery. At the outlet of wind tunnel, a frequency controlled axial fan exists. A remote control unit is used to adjust the free stream velocity in the test section.

In this study, the free stream velocities, U, are 1.42 and 4.97 m/s. Corresponding Reynolds numbers, 10000 and 35000, are calculated using Equation 3.1 where C is the chord length, υ is the kinematic viscosity of air at the free stream temperature.

$$Re = \frac{UC}{\upsilon} \tag{3.1}$$

3.1.1. Wind Tunnel Characterization

Prior to starting the tests, characterization of the wind tunnel was made in order to control the free stream velocity in the test section. The tunnel was run for a broad range of fan speed for that purpose. For this characterization, the fan speed was expressed in terms of percentage fan power factor. The free stream velocity measurements were performed using both Laser Doppler Anemometry (LDA) and Pitot-static tube techniques at prescribed locations of the test section. In addition, pressure scanner and inclined manometer were used in Pitot - static tube setup. In order to obtain most accurate velocity data from the dynamic pressures taken from the Pitot-static tube; the geographic elevation of the laboratory, humidity and ambient temperature were taken into consideration. Velocity values between Pitot - static tube and LDA measurements had a 3 % difference at most.

Based on the measurements, average velocity and turbulence intensity values as a function of fan power is constructed as shown in Figure 3.2. A linear behavior of the free stream velocity with respect to tunnel fan power factor is evident for the values greater than 4 %, which corresponds to test section velocities starting from 0.5 to 30 m/s. In addition, the maximum turbulence intensity does not exceed 0.9 % in the test section.

3.2 Flow Measurement Techniques

3.2.1 Laser-Illuminated Flow Visualization

Laser-Illuminated flow visualization is an easy and inexpensive method to investigate the flow structure. Several materials are fed as tracer particles including

bubble, dye, smoke, oil, vapor and etc. which are needed to be in the order of 1 μm in diameter to neglect the buoyancy effect.

Most commercial smoke generators used for flow visualization are vaporized oils in laboratory. Concept ViCount Compact 1300 smoke generator used in the study is illustrated in Figure 3.3. Kerosene (paraffin) mist was used as the smoke generator in this study. The mist was mixed with pressurized carbon dioxide (CO_2).

In order to visualize flow structures such as vortices, wakes and separations, laser source and optics was used to generate laser light sheet. A green laser with 400 mW power output and 532 nm wavelength was used. Cylindrical lens was utilized to convert the laser beam to laser sheet. The experiments were conducted in two different planes which were named as cross and surface flow visualization. The experimental set up for surface flow and cross flow visualizations are sketched in Figure 3.4. In surface flow visualization, the light sheet plane was located parallel to leading edge vortices. Moreover, it was arranged perpendicular to the test section at x/C = 0.44 in cross flow visualization. The images were captured by DSLR camera. The camera was located under the test section for surface flow visualization and set parallel to leading edge vortices. To take cross flow images for cross flow visualization, the camera was set outside of the test section. Downstream of the wing, a mirror was located with an orientation of 45° to free stream.

3.2.2 Surface Pressure Measurement

For pressure measurements, a pressure scanner with 16 silicon piezo-resistive pressure sensors was used. Its pre-calibration was made over certain temperature and pressure spans by the manufacturer. Owing to the temperature sensors and the integrated microprocessor, this device can recompense the transducer outputs for sensitivity, nonlinearity, offset and thermal effects before delivering data. Therefore, the measurement system assures a resolution of ±0.003 % FS (full scale).

There were 22 holes on the wings for pressure measurement and eleven of them on each half of the wing. In order to guarantee a symmetrical pressure distribution over

the entire spanwise distance at x/C=0.44, preliminary experiments were conducted. After symmetrical pattern was provided, the pressure taps located only in one half of the wing were used to perform the measurements which were acquired at 500 Hz for 10 s time intervals. Pressure scanner was connected to the pressure taps at the tip of wings with nylon tubing. The pressure measurement system is illustrated in Figure 3.5 with relevant connections. For the purpose of minimizing the surrounding noise, the device was fastened on the table and supporters were used to hang tubing. To reduce the uncertainty in the measurements, noise values were acquired at the same acquisition time and sampling rate prior to starting each case and subtracted from actual pressure measurement data.

To express the pressure distributions on the wing surface, Equation. 3.2 was used to calculate the dimensionless pressure coefficient C_p. In the charts, the C_p values were placed as $-C_p$.

$$C_p = \frac{\overline{p} - p_\infty}{\frac{1}{2}\rho U^2} = \frac{\overline{p} - p_\infty}{p_{dyn}} \tag{3.2}$$

where

ρ : Fluid Density

U: Free Stream Velocity

$\overline{p}$: Time averaged surface pressure

p_∞: Static pressure of the flow

p_{dyn}: Dynamic pressure of the flow

3.2.3 Particle Image Velocimetry (PIV) Measurements

A global characterization and detailed insight of the flow structure on delta wings can be broadened by Particle Image Velocimetry (PIV). For this reason, last measurements of experiments were done with PIV and the cases were selected after evaluation of the pressure measurement results. Over a region of interest, a series of instantaneous velocity fields is provided with this non-intrusive technique, PIV.

In present study, the global instantaneous velocity fields were obtained by utilizing TSI 2D PIV system. The system is able to generate laser pulse using a laser with the maximum repetition rate of 15 Hz. The PIV camera is an 8-bit, digital, CMOS camera with a pixel resolution of 2048 x 2048. 200 image pairs were taken per case. A fog generator was used to provide seeding particles to experimental environment.

The experimental set-up is sketched in Figure 3.6. For cross flow velocity measurement, the laser sheet was positioned perpendicular to the freestream at the selected location x/C=0.44 as the pressure measurements were carried on before. The camera was also located out of the test section perpendicular to laser plane. Inside the test section, a rectangular mirror, with dimensions of 15 x 25 cm and an angle of 45^o to the flow, was mounted eleven chord distance downstream of the delta wing. For surface flow velocity measurement, the laser sheet was positioned parallel to the delta wing surface at the selected locations. The camera was also located under the test section whose circular lens surface was positioned parallel to the delta wing surface. In addition, surface flow measurements were taken at certain distances from surface 2 (for t/C= 0.0475) and 3 (for all other wings) millimeters which correspond to distance-to-chord ratios as z/C= 0.028 and 0.042.

Insight 4G software was used to control the PIV setup. For cross flow velocity measurement, two laser pulses had 90 μs separation time (Δt) between each other. The camera has an aperture setting of f#5.6. For post processing of the cross flow PIV measurements, regions of interest of 220.1 x 42.3 mm, 211.7 x 42.3 mm for $\alpha=6^o$ and 228.6 x 42.3 mm, 232.8 x 42.3 mm for $\alpha=10^o$ were selected. The effective

grid sizes, for an interrogation window of 16 x 16 pixels, were Δ/C= 0.025 and Δ/C= 0.026 for α=6º and α=10º, respectively. For surface flow velocity measurement, the separation time (Δt) was adjusted values between 90 μs and 180 μs for different cases. For post processing of the surface flow PIV measurements, regions of interest of 406.4 x 401.6 mm for α=6º and 414.9 x 423.3 mm for α=10º were selected. The corresponding effective grid sizes, for an interrogation window of 32 x 32 pixels, were Δ/C= 0.033 and Δ/C= 0.032 for α=6º and α=10º, respectively.

3.3 Wing Models

In the experiments, four delta wing models of 35º sweep angle with t/C ratio varying from 4.75 % to 19 % are tested at angles of attack 4, 6, 8, and 10 degrees for Reynolds numbers Re=10,000 and 35,000.

Four delta wing models of 35º sweep angle with sharp edges were used in the experiments. They all had same chord of 105 mm, span of 300 mm with a bevel angle of 45º on the windward side. The thicknesses of the wings were 5 mm, 10 mm, 15 mm and 20 mm which correspond to thickness-to-chord ratios as t/C = 0.0475, 0.095, 0.1425 and 0.19, respectively. They were produced with fine polyamide PA2200 by using rapid prototyping machine in BİLTİR Center at METU. CAD drawings of the four designed models are illustrated in Figure 3.7.

A simple mount mechanism was used to provide desired position of the wing in the test section without intrusion to the upstream flow. The mount and the view of the wing is illustrated in Figure 3.8.

The wings were designed by considering the pressure measurement holes on their surfaces and considering blockage ratio. The maximum blockage ratio was 1.29 % at the highest angle of attack α=10º. The wings had 22 pressure taps with 1.5 mm diameter, which were symmetrically distributed on one spanwise station located at x/C = 0.44. Besides the pressure taps, two smoke-injection holes were placed in the vicinity of the apex to inject the smoke to the flow field, which were required for

the flow visualization experiments. The actual pictures of the wings are shown in Figure 3.9.

3.4 Experimental Matrices

In the present study, the experimental matrix was categorized under two groups: First of all, laser-illuminated smoke visualization and pressure measurement techniques were applied broadly for four delta wing models to characterize the main flow structure and foresee further cases to apply other experimental techniques in detail. The detailed sketch of the experimental matrices is presented in Figure 3.10. The smoke visualizations were performed using four delta wing models for Re=10000 and Re=35000 at angles of attack α=4°, 6°, 8° and 10°. The pressure measurements were then conducted only for Re=35000 due to the high uncertainty values obtained at relatively lower pressure readings of Re=10000. For the global characterization, the lowest and highest t/C ratio cases were selected to quantify the flow fields using PIV measurements, where the cross flow and near surface planes were utilized at angles of attack α=6° and 10° for Re=35000.

3.5 Uncertainty Estimates

In the current study, the uncertainty values associated with pressure measurement and particle image velocimetry (PIV) are calculated.

The uncertainty of surface pressure measurements related to pressure coefficients were estimated using the method given in study of Kline and McKlintock [68].

$$\omega_R = \left[\left(\omega_{x_1}\frac{\partial R}{\partial x_1}\right)^2 + \left(\omega_{x_2}\frac{\partial R}{\partial x_2}\right)^2 + \cdots + \left(\omega_{x_n}\frac{\partial R}{\partial x_n}\right)^2\right]^{1/2} \qquad (3.3)$$

In Equation 3.3, the resultant uncertainty is calculated where ω_{x_i} is the uncertainty of each independent variables. All ω_{x_i} values can be ω_p since the same scanner was

used for measurements. Equation 3.4 is used to calculate relative uncertainty of each case with a measurement accuracy of the pressure scanner of 0.05 % FS.

$$\frac{\omega_R}{R} = u_R \tag{3.4}$$

Equation 3.2 was used to calculate the pressure coefficients.

$$C_p = \frac{\overline{p} - p_\infty}{\frac{1}{2}\rho U^2} = \frac{\overline{p} - p_\infty}{p_{dyn}}$$

Applying the method above would lead to

$$\omega_{C_p} = \left[\left(\omega_p \frac{\partial C_p}{\partial \Delta P}\right)^2 + \left(\omega_p \frac{\partial C_p}{\partial p_{dyn}}\right)^2\right]^{1/2} \tag{3.5}$$

The differentiation becomes:

$$\omega_{C_p} = \left[\left(\frac{\omega_p}{p_{dyn}}\right)^2 + \left(\frac{\omega_p \Delta P}{{p_{dyn}}^2}\right)^2\right]^{1/2} \tag{3.5}$$

The calculations are made with MATLAB code in Appendix A and the results are presented in Table 1 for peak values of $-C_p$ values. The relative uncertainty value for the pressure coefficient $-C_p$ were estimated as 1.48 % at the peak values and 11.05 % for the lowest values.

Table 1 Uncertainty values for the pressure measurements at the peak values for all wings at Re=35000 for angles of attack α=4°, 6°, 8° and 10°.

Uncertainty (%)		t/C=0.0475	t/C=0.095	t/C=0.1425	t/C=0.19
α=4°	Re=35000	1.81	1.59	1.51	1.48
α=6°	Re=35000	1.57	1.55	1.49	1.55
α=8°	Re=35000	1.51	1.56	1.54	1.58
α=10°	Re=35000	1.55	1.59	1.63	1.68

For PIV measurements, Insight 4G calculates the uncertainty values by using the Peak Ratio (PR) uncertainty method. In this method, the uncertainty is determined by using peak to noise peak ratio (PPR) and the method has numerous possible sources of error including pixel displacement, seeding particles and pre-processing of the images. Further details are well described in the Insight 4G Manual [69].

The uncertainty values for PIV measurements are tabulated for the selected cases in Table 2. The maximum uncertainty value in measured velocity values is 7.04 %.

Table 2 Uncertainty values for the PIV measurements for thinnest and thickest wings at Re=35000 for angles of attack α=6° and 10°.

Uncertainty (%)		t/C=0.0475 Surface Flow	t/C=0.19 Surface Flow	t/C=0.0475 Cross Flow	t/C=0.19 Cross Flow
α=6°	Re=35000 (4.97 m/s)	7.04	5.84	7.04	6.24
α=10°	Re=35000 (4.97 m/s)	5.03	3.92	6.04	7.04

(a)

(b)

Figure 3.1 View of (a) wind tunnel facility and (b) test section.

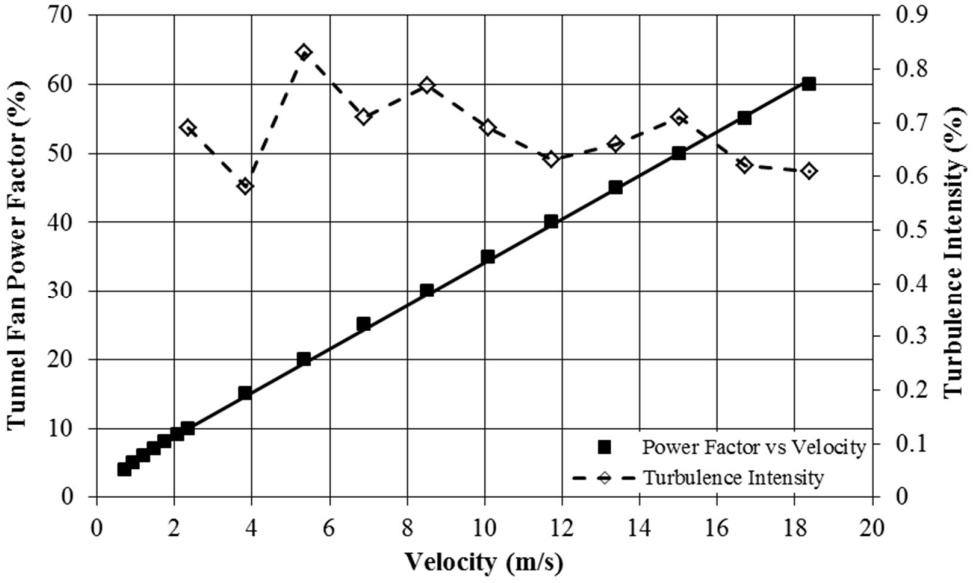

Figure 3.2 Wind tunnel calibration graph.

Figure 3.3 Photo of the smoke generator (Concept ViCount Compact 1300).

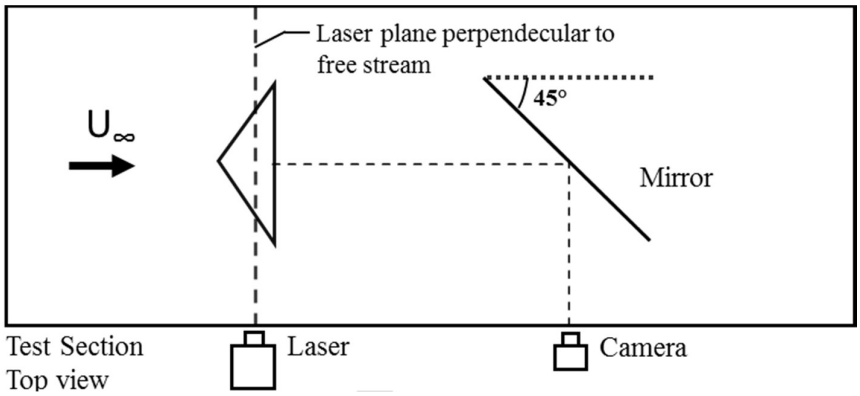

(a)

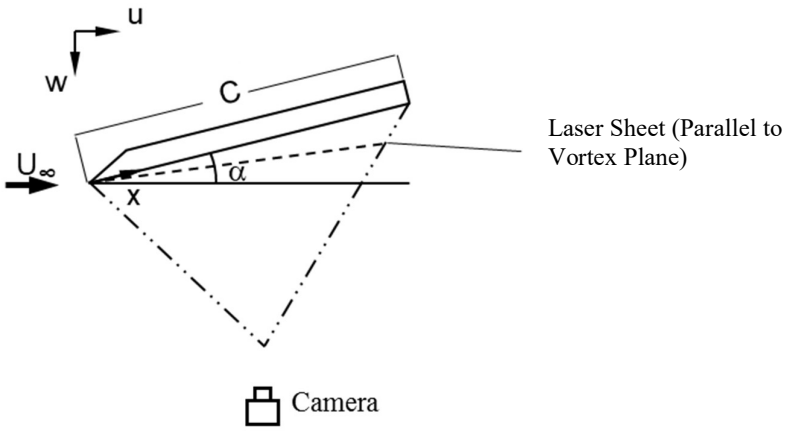

(b)

Figure 3.4 Schematics of (a) cross and (b) surface flow laser-illuminated smoke visualization experiment set-up.

(a)

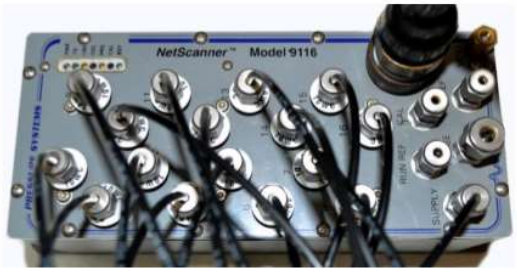

(b)

Figure 3.5 The Pressure measurement system: (a) tubing and (b) pressure scanner (Netscanner 9116 Intelligent).

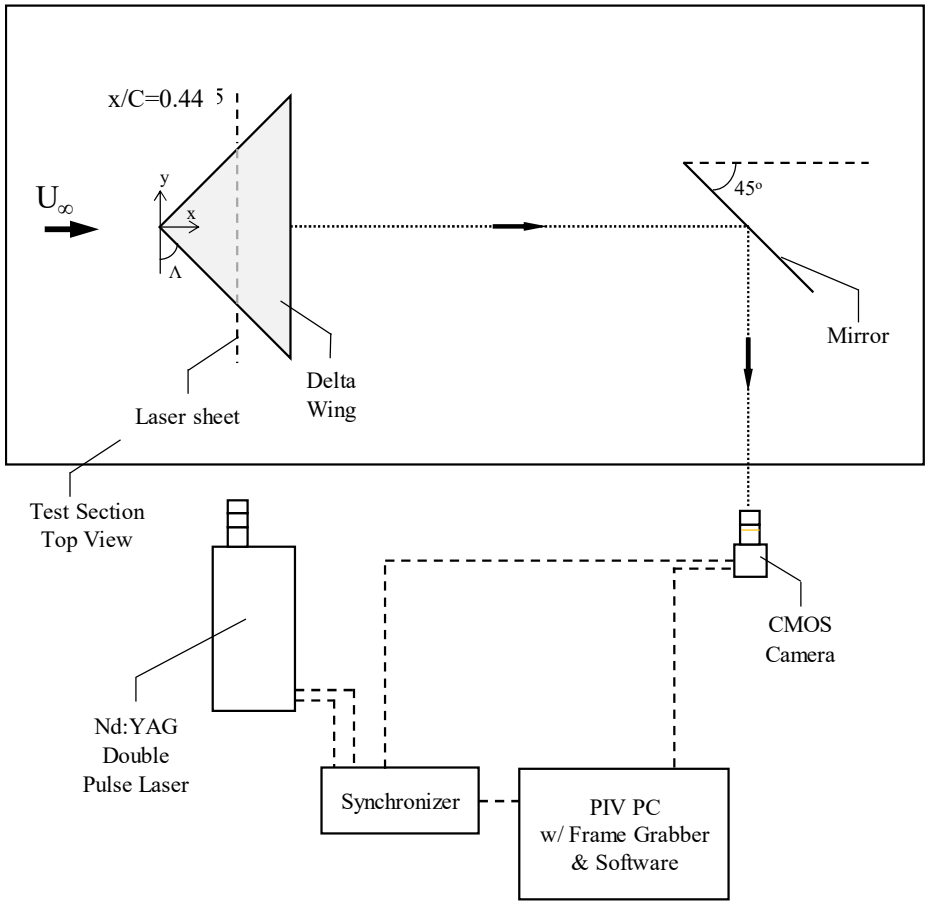

(a)

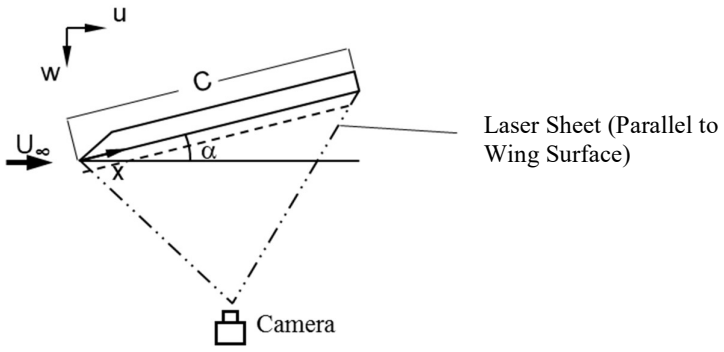

(b)

Figure 3.6 Schematic representation of the cross and surface flow PIV experiment set-up.

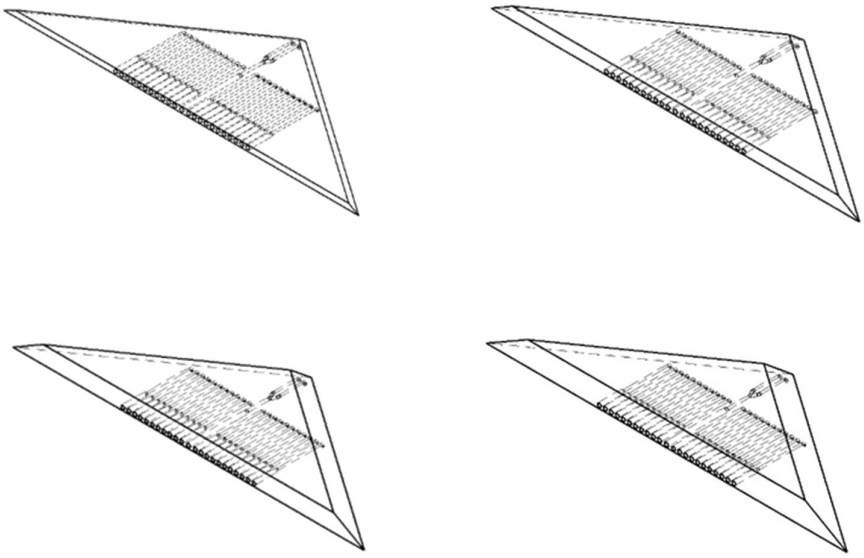

(a)

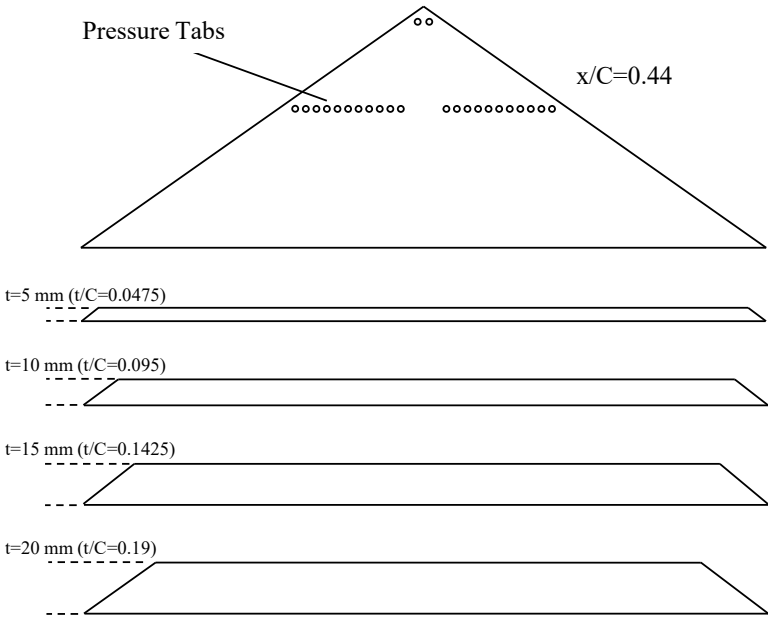

(b)

Figure 3.7 CAD drawings of the four designed models: (a) isometric view of all wings and (b) bottom view of a wing as representative and back view of all wings

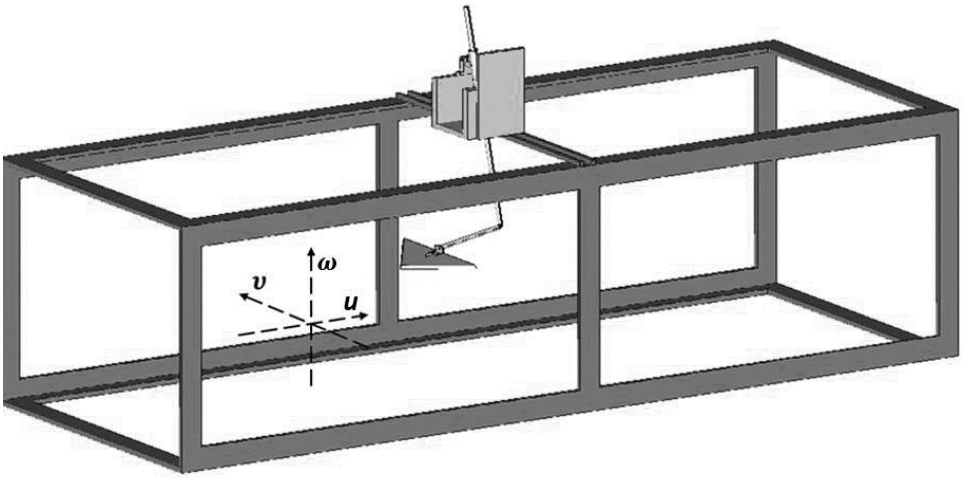

Figure 3.8 Wing model, mount and test section assembly.

Figure 3.9 Actual picture of wings from back view.

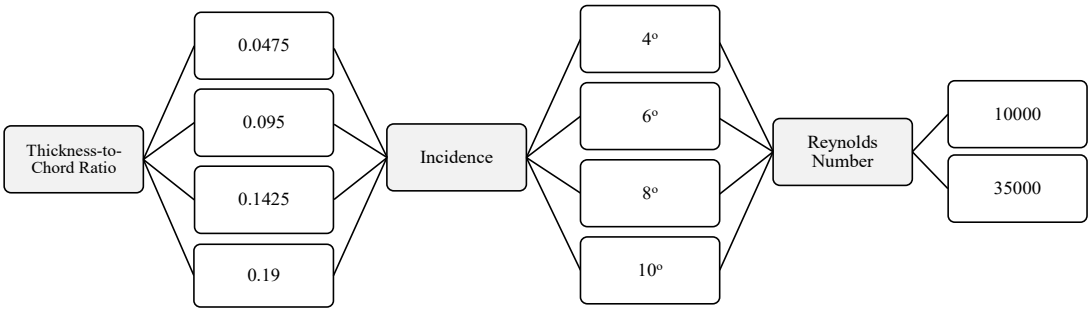

(a)

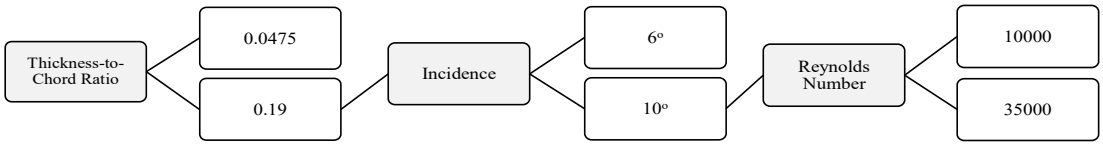

(b)

Figure 3.10 Experimental matrices for (a) surface pressure measurements & laser illuminated smoke visualizations (b) PIV measurements.

CHAPTER 4

RESULTS AND DISCUSSION

In this chapter, the results of the conducted experiments are given and discussed in detail. The chapter is divided into three parts. First, laser-illuminated flow visualizations employed for Re=10000 are reported for all t/C ratios. Then, the pressure measurements for Re=35000 are presented for all t/C ratios. At the end, the results of flow visualization, surface pressure measurement and PIV measurements including time-averaged streamlines $< \psi >$, the time-averaged velocity vectors $< V >$ and the constant contours of- vorticity $< \omega >$ are compared for t/C=0.0475 and t/C=0.19.

4.1 Surface and Cross Flow Visualization Results

The surface and the corresponding cross flow visualizations at x/C=0.44 for thickness-to-chord (t/C) ratios of 0.0475, 0.095, 0.1425, 0.19 at Reynolds number Re=10000 for the angles of attack α=4°, 6°, and 8° are demonstrated in Figure 4.1, 4.2, and 4.3, respectively. The figures are constructed in the same way for these figures such that (t/C) ratios of 0.0475, 0.095, 0.1425, and 0.19 are presented in each row from top to bottom in ascending order.

Figure 4.1 shows the results for angle of attack α=4°. The top figure represents the result of the wing, which has the thickness-to-chord ratio t/C=0.0475. Smoke traces demonstrate that there is dual vortex structure, where the vortex breakdown takes place in the vicinity of the trailing edge for the primary vortex. The relatively weaker vortex structure, second primary vortex, breaks down close to mid-chord.

When thickness-to-chord ratio reaches to t/C=0.095, more dispersed dual vortex structure is observed compared to the wing with t/C=0.0475. As the t/C ratio

increases from t/C=0.0475 to t/C=0.095, the whole vortical structures move toward the symmetry plane.

Considering the results of thickness-to-chord ratio t/C=0.1425, both the surface and cross flow smoke patterns indicate deterioration in the vortical structures such that dual vortex structure is not apparent and leading edge vortex do not represent standard formation.

As the thickness-to-chord ratio increases to t/C=0.19, the level of the deterioration significantly increases. There is no clear indication of leading edge vortex and vortex breakdown, which might be due to the localized small-scale separations on the wing surface.

Considering the smoke visualization results of complete set of t/C ratios as shown in Figure 4.1, as the t/C ratio increases, the flow structure transform into a complete different phase of localized separated flow regime from the dual vortex structure. In addition, it is important to note that, with increasing t/C ratio, the thickness of the flow structure, which is the separated shear layer from the windward side of the wing, increases significantly and the flow structure moves toward the symmetry plane.

The surface and the cross flow visualizations for angle of attack $\alpha=6^{o}$ are demonstrated in Figure 4.2. Considering the results of t/C=0.0475 shown in the top row, dual vortex structure is apparent in the flow field. As the t/C ratio increases to t/C=0.095, the smoke traces on the surface indicate large-scale swirl structure rather than the leading edge vortex structure. This structure is a typical representation of large-scale, three-dimensional surface separation. Further increase in t/C ratio to t/C=0.1425 and t/C=0.19 enlarges the scale of the swirl pattern and moves the center of this swirl pattern toward the trailing edge of the wing.

The corresponding results of near and surface smoke visualizations for angle of attack $\alpha=8^{o}$ are presented in Figure 4.3. Considering the result for the thickness-to-chord ratio t/C=0.0475 as shown in the top images, the smoke traces on the surface

indicate large-scale swirl structure, which correspond to three dimensional surface separation. As discussed in the results for angle of attack α=6°, increase in t/C ratio enlarges the scale of the swirl pattern and moves the center of this swirl pattern toward the trailing edge of the wing for angle of attack α=8° as shown in Figure 4.3.

Additional surface and cross flow smoke visualization results are presented in Appendix B including the case for the angle of attack α=10° at Reynolds number Re=10000 and the cases at angles of attack α=4°, 6°, 8° and 10° for Reynolds number Re=35000.

4.2 Surface Pressure Measurement Results

The mean surface pressure values in terms of the dimensionless pressure coefficient $-C_p$ against non-dimensional spanwise distances at chordwise location of x/C=0.44 are demonstrated at four different angles of attack α=4°, 6°, 8° and 10° at Reynolds number of Re=35000 in Figure 4.4. The dimensionless spanwise distance, y/S, is from the wing symmetry plane, where S is the half spanwise distance located at x/C=0.44. Each chart in Figure 4.4 corresponds to a single angle of attack and represents the $-C_p$ values for t/C ratios 0.0475, 0.095, 0.1425, and 0.19. In the charts, high $-C_p$ values indicate suction and likely to represent the region of vortex core, whereas, low $-C_p$ values indicate the regions where the flow possibly attaches to the wing surface.

Considering the results for the angle of attack α=4° as shown in top left chart in Figure 4.4, the pressure distribution for all cases exhibits the footprint of the vortical structure. Increase in thickness-to-chord ratio causes an increase in the suction behavior of the vortical flow for which the highest $-C_p$ value for all cases is approximately coincident at y/S= 0.45. For t/C= 0.0475, the value of the highest $-C_p$ is found as 0.73 whereas for t/C=0.095 yields 22 % percent increase in the highest $-C_p$ value. This increase indicates a stronger vortex structure that means higher lift for the wing. Further increasing the thickness-to-chord ratio to t/C= 0.1425 and t/C= 0.19 exhibits a similar distribution with the highest $-C_p$ value

around 1.00. Similar to a region of highest $-C_p$ values, a region of lowest $-C_p$ values proximity to the center of the wing is considered to represent flow attachments to the wing surface. Pressure distributions indicate that the flow reattachments move slightly toward the symmetry plane from y/S=0.32 to y/S=0.24 as the t/C ratio increases.

The pressure distribution for the angle of attack α=6° is shown in the bottom left chart of Figure 4.4, which represents a footprint of vortical structure and has similar peak $-C_p$ values. Considering the locations of the highest and the lowest $-C_p$ values, which correspond to the vortex core and reattachment on the wing surface, the highest $-C_p$ value appears at around y/S= 0.45 for all cases as in the lower angle of attack α=4°, whereas the reattachment region move toward the symmetry plane from y/S=0.32 to y/S=0.16 as the t/C ratio increases.

Considering the results for the angle of attack α=8° as shown in top right chart in Figure 4.4, the pressure distribution demonstrates the typical footprint of vortical structure on the wing surface for t/C= 0.0475 and t/C= 0.095. As the t/C ratio increases, the pressure distribution turns in to more flat profile where the difference in the magnitude of the highest and lowest $-C_p$ value, ΔC_p, drops significantly. This is an indication of drop in the strength of leading edge vortex.

Considering the results for the angle of attack α=10° as shown in bottom right chart in Figure 4.4, the wing models with t/C= 0.1425 and t/C= 0.19 have flat-like $-C_p$ distributions, which are the indications of three-dimensional separated flow over the wings. However, the wing model with t/C=0.0475 demonstrates the typical representation of the vortical structure. The results indicate that the effect of t/C ratio on flow structure is quite substantial such that for the same attack angle the wing might expose to leading edge vortex structure or three dimensional separated flow regime depending on the t/C ratio.

Figure 4.5 is constructed using the same $-C_p$ distributions to further discuss the aforementioned results. Each chart in Figure 4.5 corresponds to a single t/C ratio

and represents $-C_p$ values for the angles of attack α=4°, 6°, 8°, and 10°. Without discussing the details of each chart, the global comparison of two figures, Figures 4.4 and 4.5, are made. The charts of both figures demonstrate very similar distributions, which means that fixing the angle of attack and varying the t/C ratio induces almost identical distributions with fixing the t/C ratio and varying the angle of attack within the ranges of parameters tested in the present study. This is quite important in terms of demonstrating the significance of the effect of t/C ratio on flow structure.

4.3 Detailed Comparison of t/C=0.0475 and t/C=0.19 using Flow Visualization, Surface Pressure Measurement, and PIV Measurements

In order to further characterize the t/C ratio, the results of minimum and maximum t/C ratio wings as t/C=0.0475 and t/C=0.19 at Reynolds number of Re=35000 are presented in Figure 4.6 and 4.7 for angle of attack α=6° and in Figure 4.8 and 4.9 for angle of attack α=10°. In Figure 4.6 and 4.8, near surface flow time-averaged velocity vectors $< V >$, streamline patterns $< \Psi >$, and constant contours of surface normal vorticity $< \omega >$, along with the surface-flow visualizations are demonstrated. In Figure 4.7 and 4.9, the surface pressure distributions, cross flow time-averaged velocity vectors $< V >$, streamline patterns $< \Psi >$, and constant contours of axial vorticity $< \omega >$, along with the cross-flow visualizations are demonstrated. The figures are constructed such that the left images indicate the results of t/C=0.0475 where the right images correspond to the results of t/C=0.19. The dash lines in near surface flow measurements and surface visualizations indicate corresponding cross flow planes at x/C=0.44.

Considering the results in Figure 4.6, surface flow visualization shows that a leading edge vortex is apparent for both wings. The constant contours of surface normal vorticity demonstrate that the vorticity concentration slightly moves toward the symmetry plane as t/C ratio increases to t/C=0.19. According to the patterns of streamline topology, well-defined features are observed. For both cases, a positive

bifurcation line BL^+ represents a line of attachment which streamlines tend to diverge. When thickness-to-chord ratio reaches to t/C=0.19, a positive bifurcation line BL^+ moves toward to centerline of the wing planform. A negative bifurcation line BL^- extents along the leading edge of the wing that corresponds to a line of separation for both wing surfaces. Streamlines tend to converge in the nodal points N, which are the points that BL^- terminates near the apex. By increasing t/C to 0.19, N moves toward to apex of the wing. In addition, streamlines tend to move opposite directions on the wing surface at the saddle point S which is observed to move toward trailing edge with an increase in t/C ratio. The results of time-averaged velocity vector for near surface flow measurements represent that, the magnitude of the velocity vector decreases downstream of the leading-edge for both cases. As the value of t/C increases from 0.0475 to 0.19, the spatial extent of the region of very low velocity increases. Considering the details of each sub-figure in Figure 4.6, it is important to note that, smoke traces, vortex patterns and patterns bifurcation lines are in agreement with eachothers in each case.

The results of $-C_p$ distributions in Figure 4.7 represent a footprint of vortical structure for both wings with similar peak $-C_p$ values. The locations of the highest and the lowest $-C_p$ values show that the highest $-C_p$ value is observed at around y/S= 0.45 for both cases, whereas the reattachment region move toward the symmetry plane from y/S=0.32 to y/S=0.16 with increasing t/C ratio. The results of cross flow visualization and PIV measurements are consistent with the results of $-C_p$ distributions. Smoke traces, the constant contours of axial vorticity, streamline patterns and velocity vectors demonstrate vortical flow for both wings. The location of the vortex core slightly moves toward the centerline of the wing with increase of t/C ratio to 0.19. The results of the axial vorticity contours show that the level of the vorticity decreases 13% in the peak value by increasing the t/C ratio to t/C=0.19. The velocity vectors also show a decrease in magnitude along with the increase in t/C ratio.

Considering the results in Figure 4.8, surface flow visualization shows that the wing with t/C=0.0475 experiences vortical flow with an apparent reattachment whereas the smoke traces demonstrate large-scale swirl structure, which correspond to three dimensional surface separation for the wing with t/C=0.19. The surface normal vorticity contours demonstrate significant difference on levels between the wings with t/C=0.0475 and 0.19 that corresponds to an approximate 63 % reduction in the peak value of vorticity concentration for the wing with t/C=0.19. The results of streamline topology pattern represent that the node N of the wing with t/C=0.0475 gives way to a large-scale focus F for the wing with t/C=0.19. The relation between F at the surface and the flow away from the surface corresponds to development of a three-dimensional vortical structure. In addition, there exists another focal point beyond the trailing edge. An increase in t/C ratio causes movement of this focal point F slightly far away from the trailing edge. By increasing the thickness-to-chord ratio to t/C=0.19, the reattachment reaches the centerline of the wing. A negative bifurcation line BL^{-} on the surface of the wing with t/C=0.19 moves toward the leading edge of the wing. Besides aforementioned flow aspects, a saddle point S is observed to move beyond the trailing edge with an increase in t/C ratio. According to the time-averaged velocity vector, the magnitude of the velocity decreases downstream of the leading-edge for both wings. The increase in thickness-to-chord ratio results in a decrease of the magnitude of the velocity. In addition, the spatial extent of very low velocities increases as the thickness-to-chord ratio increases.

The results of $-C_p$ distributions in Figure 4.9 represent a typical representation of the vortical structure for the wing with t/C=0.0475 while there is a flat-like $-C_p$ distribution for the wing with t/C=0.19 which is indication of three dimensional surface separation. Cross flow visualization shows that a vortical flow structure is evident for t/C=0.0475 whereas the flow is completely dispersed over the half-spanwise distance of the wing with t/C=0.19. The constant contours of axial vorticity demonstrate an approximate 75 % reduction in vorticity levels along with

an increase in t/C. Streamline patterns and velocity vectors show that the vortical core slightly moves inboard of the symmetry plane. Magnitude of the velocity vectors in the vicinity of the vortex core decreases as t/C ratio increases to t/C=0.19. For a detailed investigation, comparison of individual cross flow PIV results of wings having t/C=0.0475 and 0.19 are presented for $\alpha=6^{o}$ and $\alpha=10^{o}$ in Appendix B, Figures B.6 and B.7, respectively. Likewise, comparison of individual surface flow PIV results of wings having t/C=0.0475 and 0.19 are presented for $\alpha=6^{o}$ and $\alpha=10^{o}$ in Appendix B, Figures B.8 and B.9, respectively.

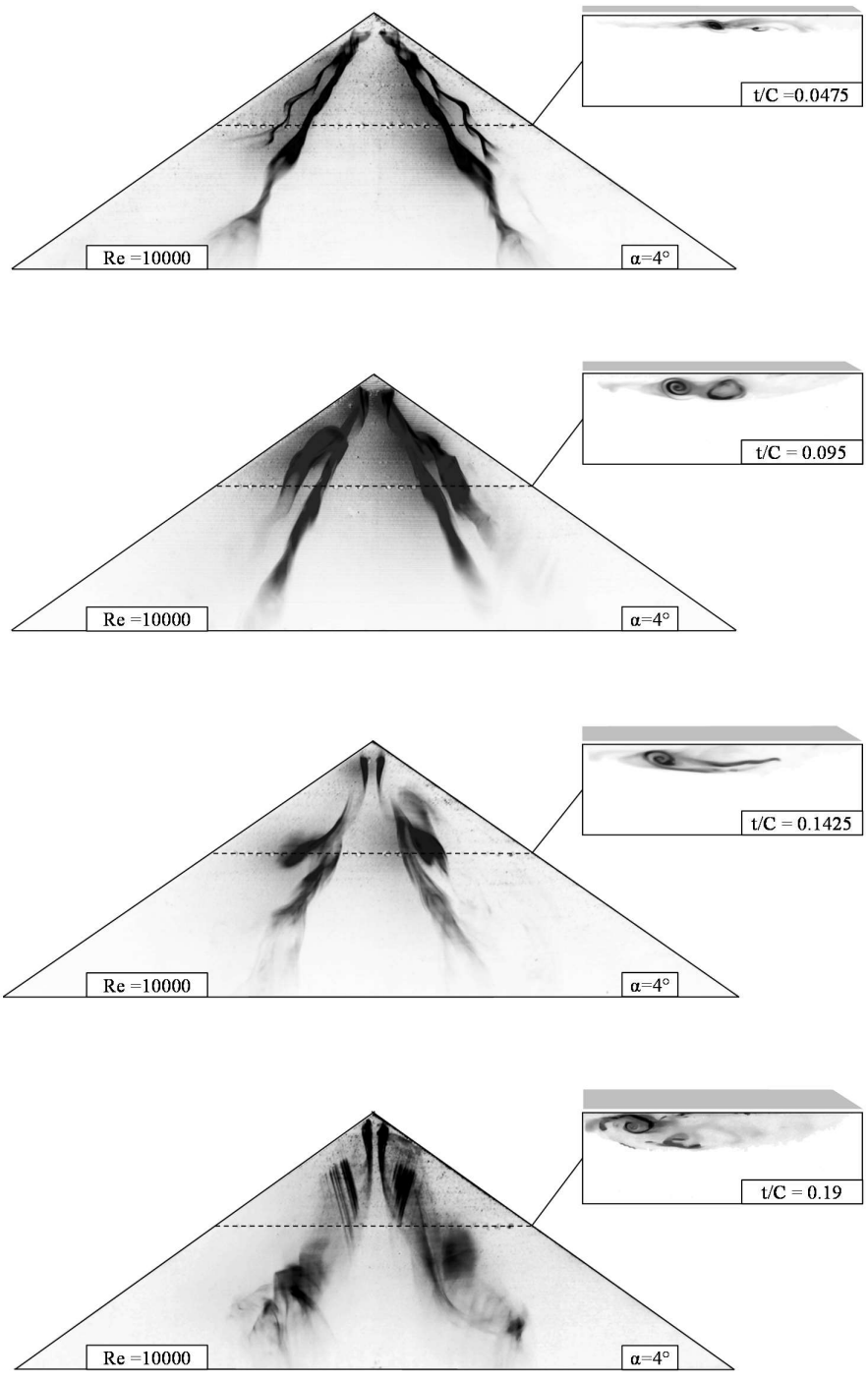

Figure 4.1 Laser-illuminated surface and cross flow smoke visualizations of t/C=0.0475, 0.095, 0.1425, 0.19 for Re=10000 at angle of attack of α=4°

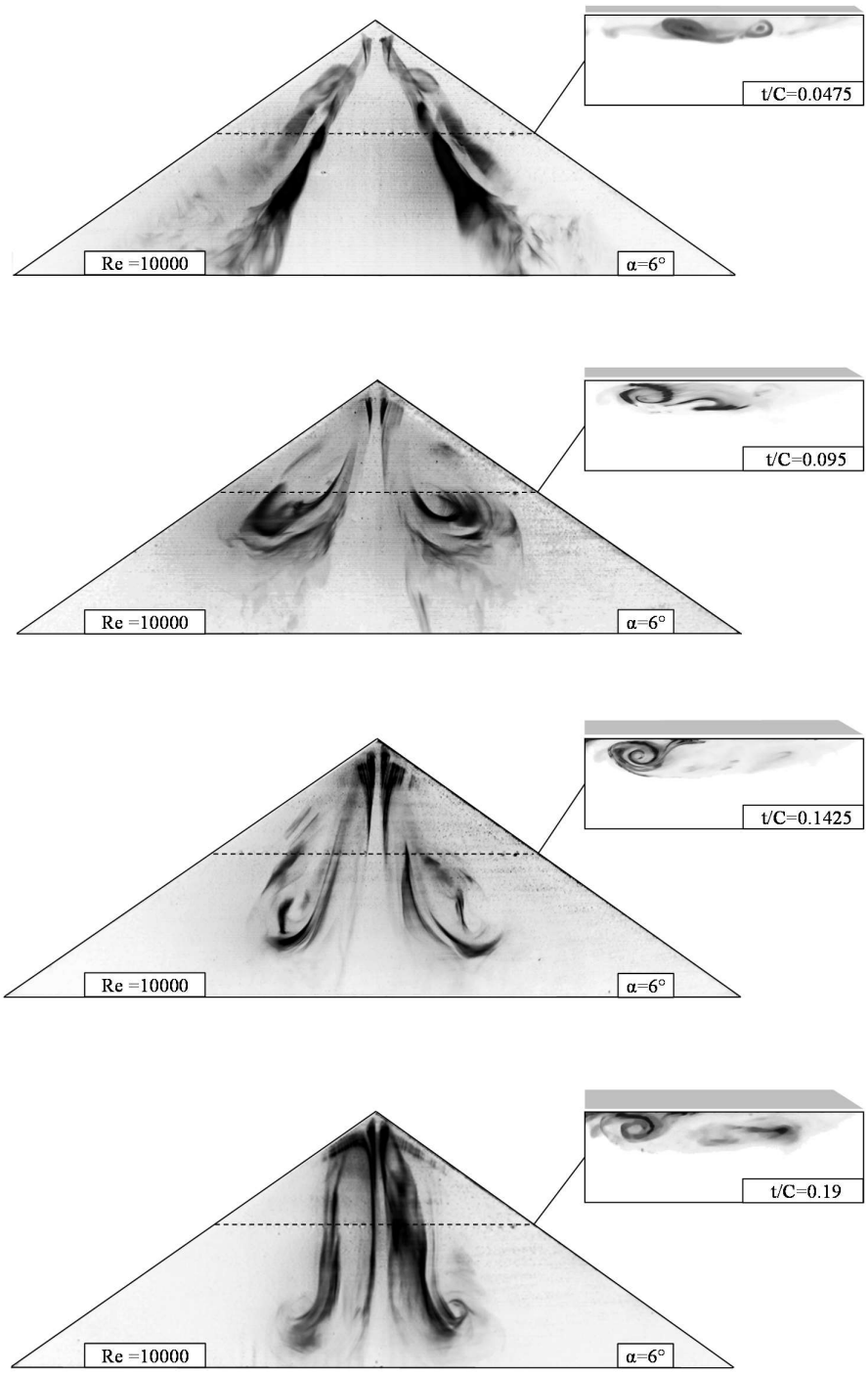

Figure 4.2 Laser-illuminated surface and cross flow smoke visualizations of t/C=0.0475, 0.095, 0.1425, 0.19 for Re=10000 at angle of attack of α=6°

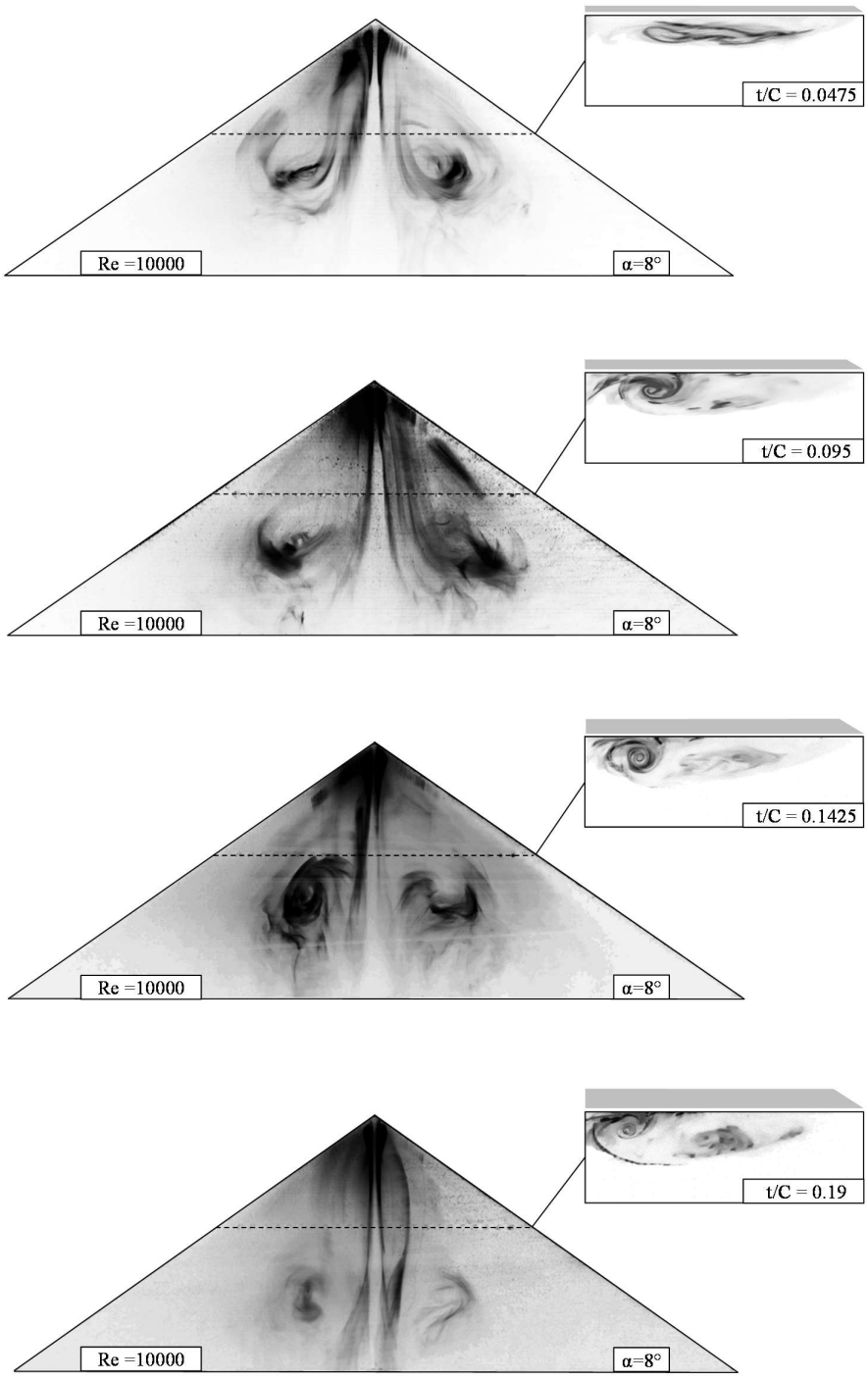

Figure 4.3 Laser-illuminated surface and cross flow smoke visualizations of t/C=0.0475, 0.095, 0.1425, 0.19 for Re=10000 at angle of attack of α=8°

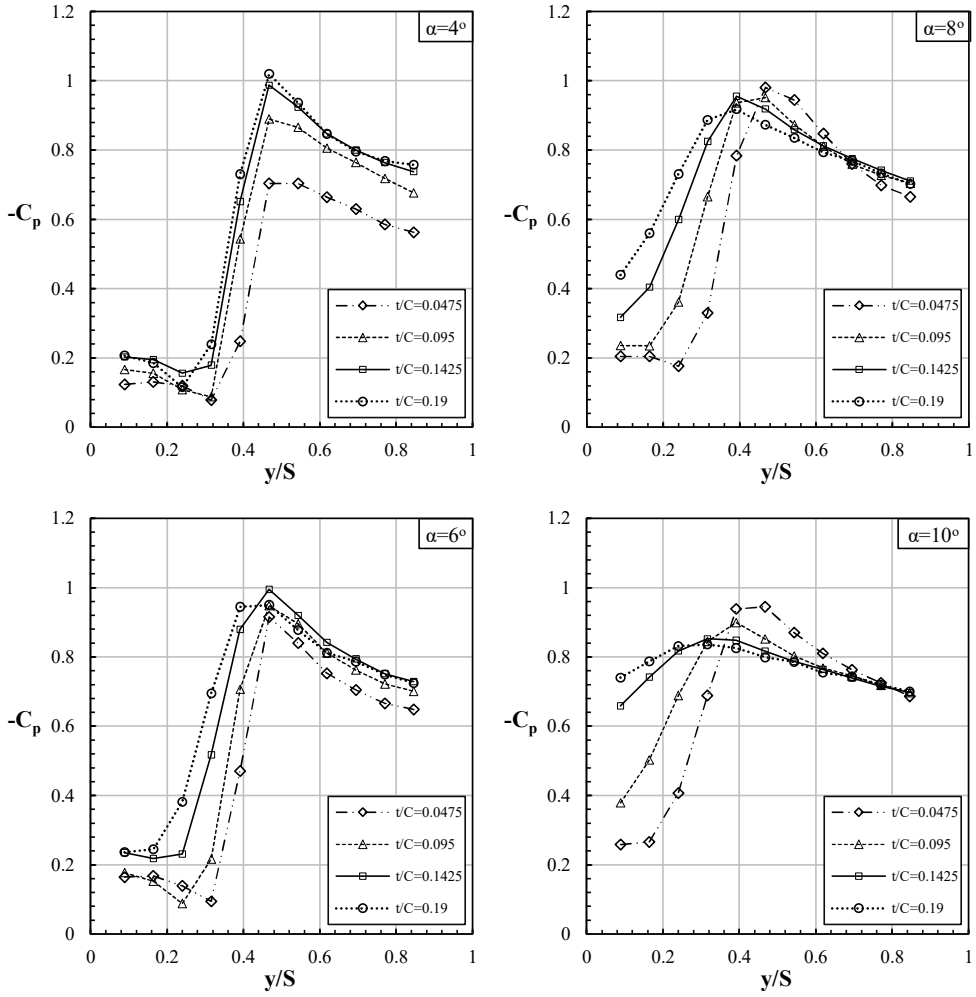

Figure 4.4 The dimensionless pressure distribution $-C_p$ of t/C=0.0475, 0.095, 0.1425, 0.19 along spanwise direction for Re=35000 at angles of attack α=4°, 6°, 8° and 10°

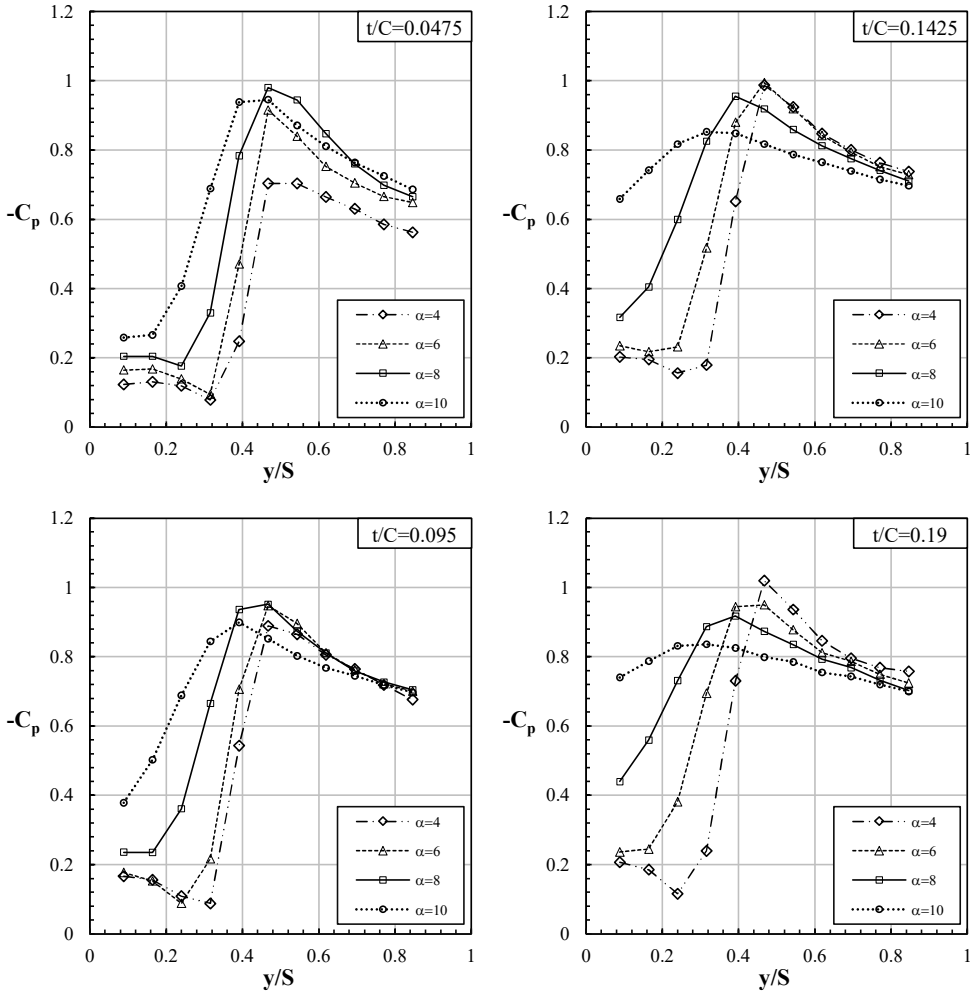

Figure 4.5 The dimensionless pressure distribution $-C_p$ of angles of attack α=4º, 6º, 8º and 10º along spanwise direction for Re=35000 at t/C=0.0475, 0.095, 0.1425, 0.19.

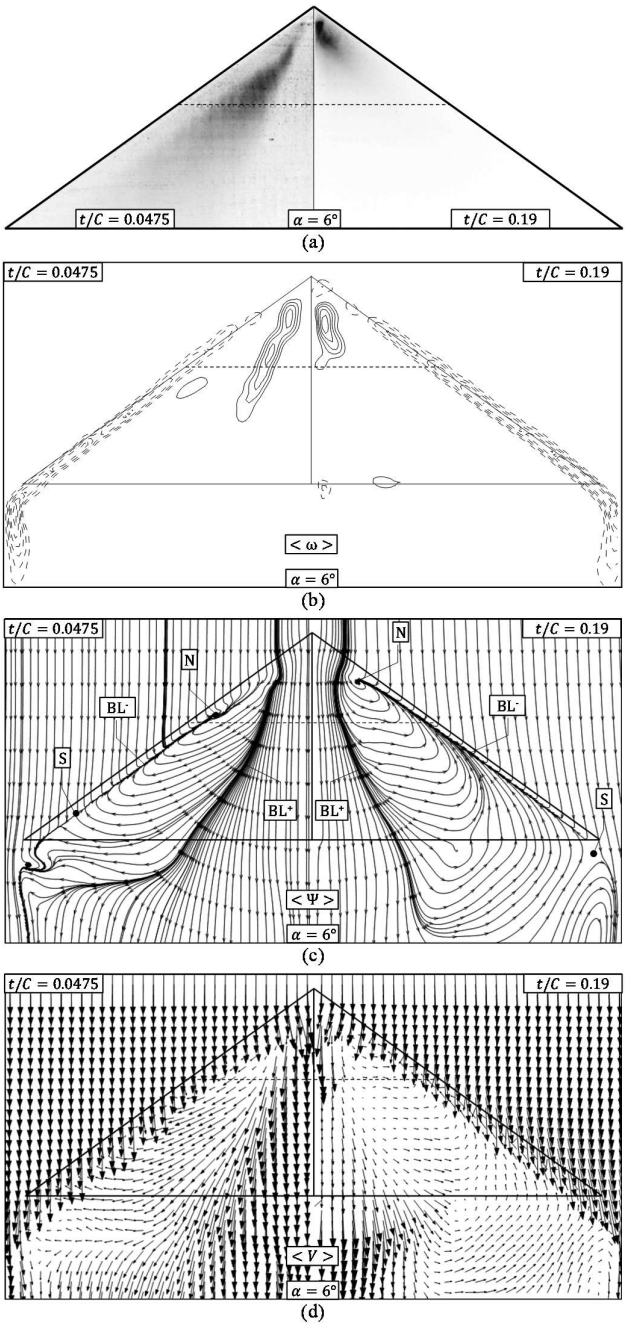

Figure 4.6 Comparison of (a) surface flow smoke visualizations with patterns of (b) time-averaged velocity vectors $\langle V \rangle$, (c) streamlines $\langle \Psi \rangle$ and (d) constant contours of surface normal vorticity $\langle \omega \rangle$ at angle of attack $\alpha = 6$ deg for $Re = 3.5 \times 10^4$ for $t/C = 0.0475$ and $t/C = 0.19$, $[|\langle \omega \rangle|]_{min} = 200$ s^{-1}, $\Delta[|\langle \omega \rangle|] = 100$ s^{-1}

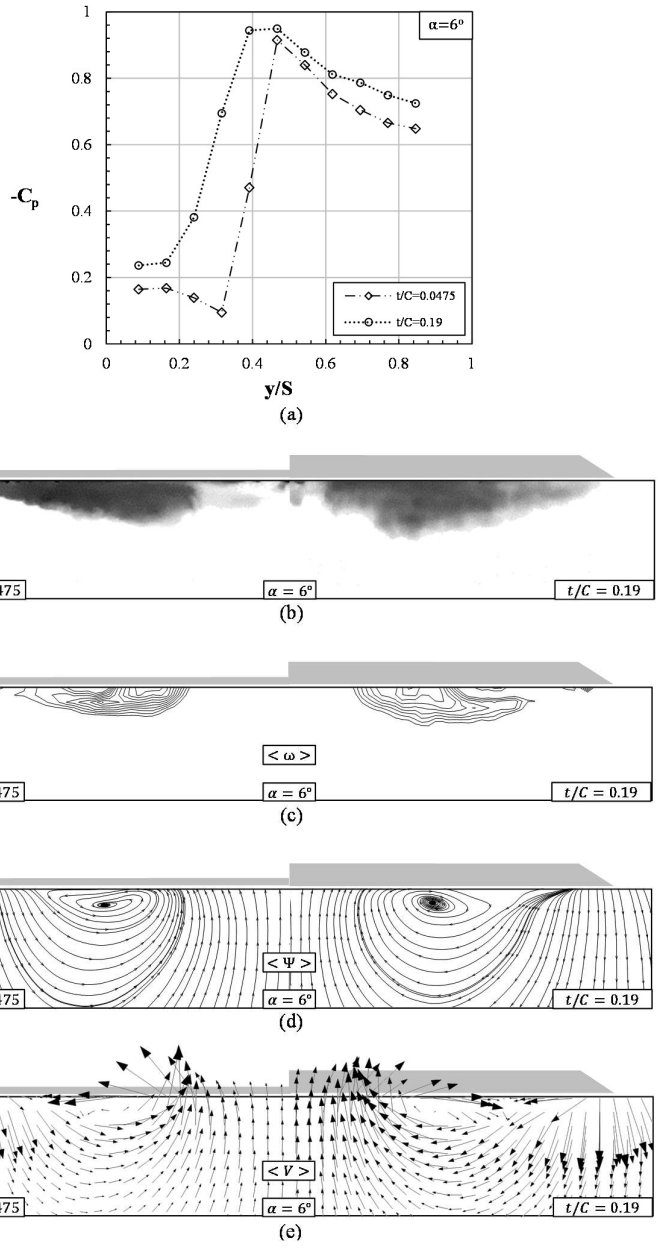

Figure 4.7 Comparison of (a) C_p distributions and (b) cross flow smoke visualizations with patterns of (c) time-averaged velocity vectors $\langle V \rangle$, (d) streamlines $\langle \Psi \rangle$ and (e) constant contours of axial vorticity $\langle \omega \rangle$ at angle of attack $\alpha = 6$ deg for $Re = 3.5 \times 10^4$ for $t/C = 0.0475$ and $t/C = 0.19$, $[|\langle \omega \rangle|]_{min} = 200$ s^{-1}, $\Delta[|\langle \omega \rangle|] = 100$ s^{-1}

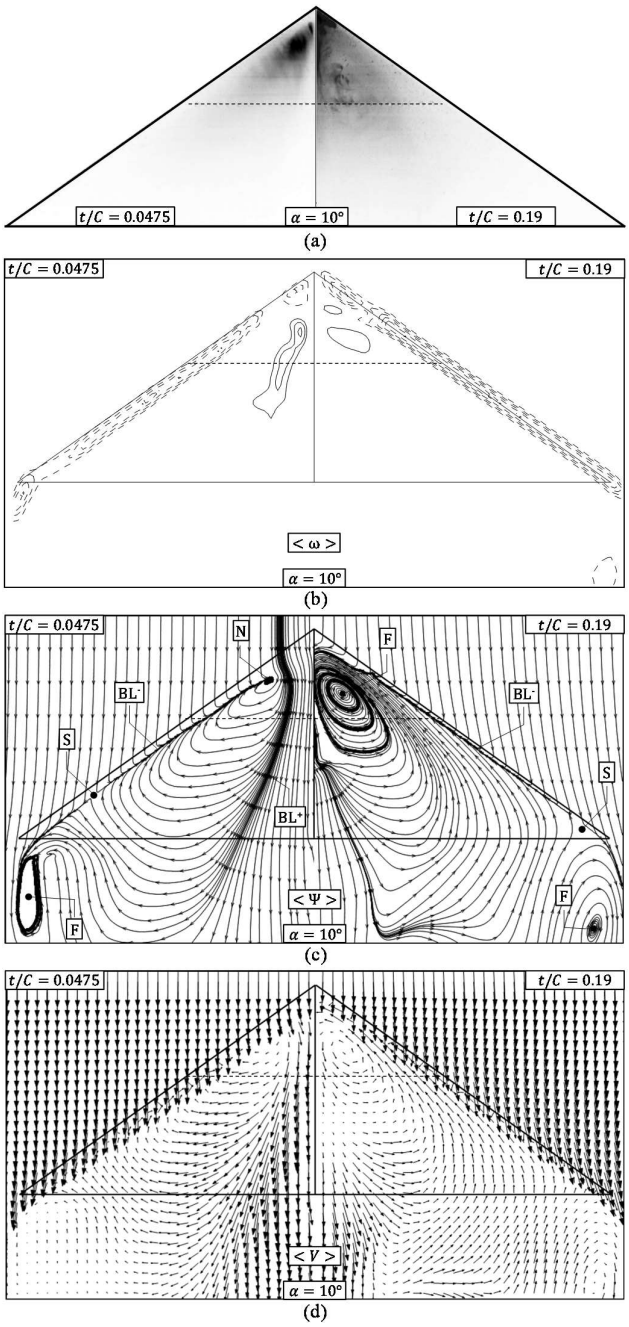

Figure 4.8 Comparison of (a) surface flow smoke visualizations with patterns of (b) time-averaged velocity vectors $\langle V \rangle$, (c) streamlines $\langle \Psi \rangle$ and (d) constant contours of surface normal vorticity $\langle \omega \rangle$ at angle of attack $\alpha = 10$ deg for $Re = 3.5 \times 10^4$ for $t/C = 0.0475$ and $t/C = 0.19$, $[|\langle \omega \rangle|]_{min} = 200$ s^{-1}, $\Delta[|\langle \omega \rangle|] = 100$ s^{-1}

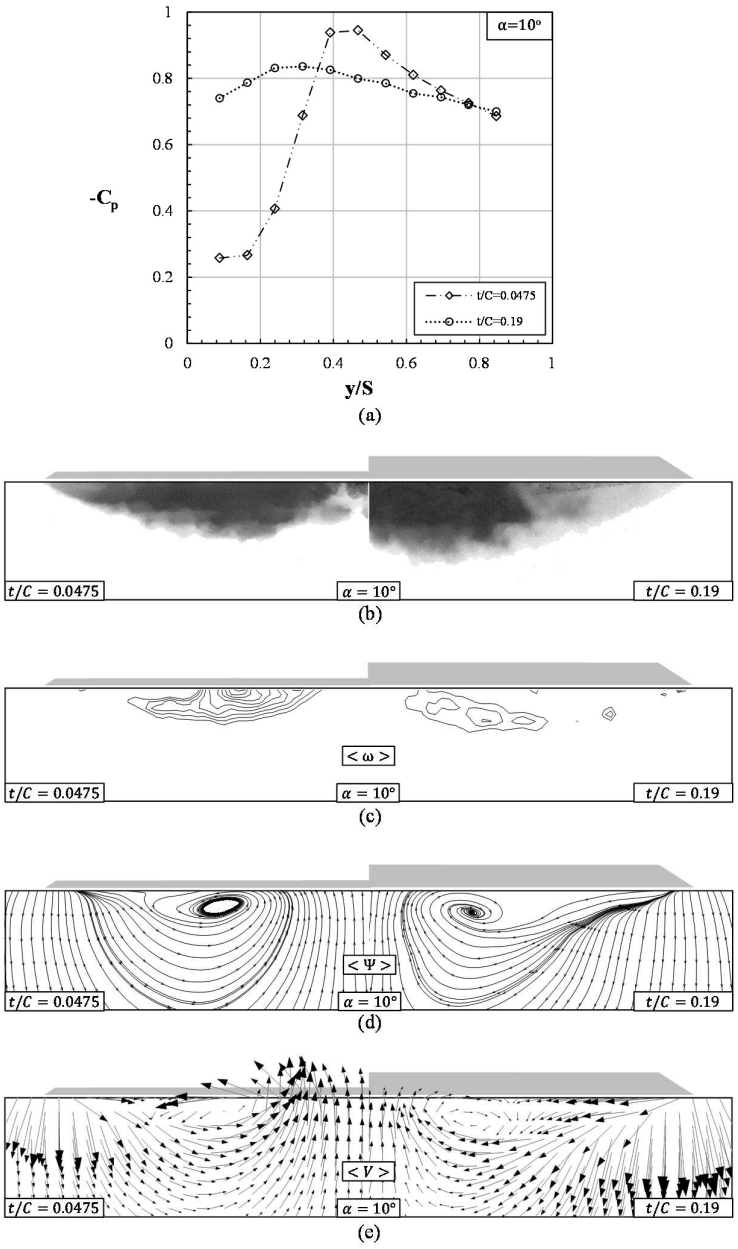

Figure 4.9 Comparison of (a) C_p distributions, and (b) cross flow smoke visualizations with patterns of (c) time-averaged velocity vectors $\langle V \rangle$, (d) streamlines $\langle \Psi \rangle$ and (e) constant contours of axial vorticity $\langle \omega \rangle$ at angle of attack $\alpha = 10$ deg for $Re = 3.5 \times 10^4$ for $t/C = 0.0475$ and $t/C = 0.19$, $[|\langle \omega \rangle|]_{min} =$ 200 s^{-1}, $\Delta[|\langle \omega \rangle|] = 100$ s^{-1}

CHAPTER 5

CONCLUSION

5.1 Summary and Conclusions

In this study, the effect of thickness-to-chord ratio on flow structure over a 35° swept delta wing was investigated by using surface pressure measurement, laser-illuminated smoke visualization and particle image velocimetry (PIV) techniques. Four identical delta wings with different thickness-to-chord ratios including 0.0475, 0.095, 0.1425, 0.19 has been examined for the angles of attack of α=4°, 6°, 8° and 10° at Re=10000 and Re=35000.

According to the results of surface and cross flow smoke visualizations at x/C=0.44 for Re=10000, following conclusions are obtained:

- At angle of attack α=4°, dual vortex structure transforms into a complete different phase of localized separated flow regime with increasing t/C ratio. It is worth mentioning that, as t/C ratio increases, the thickness of the flow structure, the separated shear layer from the windward side of the wing, increases considerably and the flow structure moves toward the symmetry plane.
- At angle of attack α=6°, large-scale swirl structure, that corresponds to three-dimensional surface separation, is observed except for the wing with t/C=0.0475 which has dual vortex structure. Increase in t/C ratio to t/C=0.1425 and t/C=0.19 enlarges the scale of the swirl pattern and moves the center of this swirl pattern toward the trailing edge of the wing. For angle of attack α=8°, large-scale swirl structure is apparent for all wings and as

observed for angle of attack α=6º, the scale of the swirl pattern enlarges and its center moves toward the trailing edge of the wing as t/C ratio increases.

The results of pressure and velocity measurements and smoke visualizations for Re= 35000 represent the following conclusions:

- $-C_p$ distributions at α=4° and α=6° show that, the pressure distribution for all cases exhibits the vortical footprint. For each angle of attack, the maximum $-C_p$ value varies around 1. In addition, the flow reattachment moves toward symmetry plane as t/C ratio increases.
- Fixing the angle of attack and varying the t/C ratio induces almost identical $-C_p$ charts with fixing the t/C ratio and varying the angle of attack within the ranges of parameters tested in the present study. This is quite important in terms of demonstrating the significance of the effect of t/C ratio on flow structure.
- As discussed for Reynolds number Re=10000, the effect of t/C ratio on flow structure is substantial such that for the same attack angle the wing might expose to leading edge vortex structure or three dimensional separated flow regime depending on the t/C ratio.

Considering the results of the present study and the related studies in literature, in the present study, an increase in t/C ratio results in stronger vortical structure and movement of reattachment line to the centerline of the wing at low angles of attack which is quite in line with the surface pressure distributions of moderate, 45 degree swept delta wing as reported by Kawazoe [19]. However, considering the relatively higher angles of attack cases which presumably correspond to pre-stall and stall conditions, the findings in both studies contradict which might be due to the differences in sweep angles and bevel shapes of the wings used in the studies.

5.2 Recommendations for Future Work

In this thesis, the effect of thickness-to-chord ratio on flow structure of a low swept delta wing has been investigated experimentally. The present study can be further improved in the following ways:

- To further understand the effect of thickness-to-chord ratio on flow structure of a low swept delta wing and to draw conclusions, t/C ratio range and the experimental matrix including Reynolds number and angles of attack need be extended.
- The effect of t/C ratio on the thickness of the flow structure on wing surface separated from the windward side of the wing need to be quantified. The link between this thickness and the flow regimes including leading edge vortex and three-dimensional surface separation should be further studied.
- To further understand the effect of t/C ratio on flow structure in detail, the effect of bevel angle needs to be quantified since the formation of vortical structure is highly affected by the shape of the leading edge and the total beveled area on the edges.
- Lift and drag force measurements should be performed to understand the effect of thickness-to-chord ratio on the aerodynamic performance of the wing.

REFERENCES

[1] I. Gursul, R. Gordnier, and M. Visbal, "Unsteady aerodynamics of nonslender delta wings," *Prog. Aerosp. Sci.*, vol. 41, no. 7, pp. 515–557, 2005.

[2] I. Gursul, "Vortex flows on UAVs: Issues and challenges," *Aeronaut. J.*, vol. 108, no. 1090, pp. 597–610, 2004.

[3] I. Gursul, Z. Wang, and E. Vardaki, "Review of Flow Control Mechanisms of Leading-Edge Vortices," *Prog. Aerosp. Sci.*, vol. 43, no. 7–8, pp. 246–270, Oct. 2007.

[4] C. Breitsamter, "Unsteady Flow Phenomena Associated with Leading-Edge Vortices," *Prog. Aerosp. Sci.*, vol. 44, no. 1, pp. 48–65, 2008.

[5] I. Gursul, "Review of Unsteady Vortex Flows over Slender Delta Wings," *J. Aircr.*, vol. 42, no. 2, pp. 299–319, 2003.

[6] J. J. Kacprzynski, H. Ashley, and R. Sankaranarayanan, "On the Calculation of Unsteady Nonlinear Three-Dimensional Supersonic," *J. Basic Eng.*, vol. 90, no. 4, pp. 581–595, 1968.

[7] A. G. Parker, "Aerodynamic Characteristics of Slender Wings with Sharp Leading Edges - A Review," *J. Aircr.*, vol. 13, no. 3, pp. 161–168, 1976.

[8] D. H. Peckham, "Low-Speed Wind-Tunnel Tests on a Series of Uncambered Slender Pointed Wings with Sharp Edges," *R&M 3186*, 1958.

[9] S. B. Berndt, "Three Component Measurements and Flow Investigations of Plane Delta Wings at Low Speed and Zero Yaw," *K.T.H. Aero. TN 4*, 1949.

[10] H. C. Garner and D. E. Lehrian, "Non-Linear Theory of Steady Forces on Wings with Leading-Edge Flow Separation," *R&M 3375*, 1963.

[11] S. A. Thompson, “The Unsteady Aerodynamics of a Delta Wing Undergoing large Amplitude Pitching Motion,” *PhD Diss. Univ. Notre Dome*, 1992.

[12] M. V Lowson and A. J. C. Ponton, “Symmetry Breaking in Vortex Flows on Conical Bodies,” *AIAA J.*, vol. 30, no. 6, p. 797, 1992.

[13] W. H. Wentz and D. H. Kohliman, “Vortex Breakdown on Slender Sharp-Edges Wings,” *J. Aircr.*, vol. 8, no. 3, pp. 156–161, 1971.

[14] R. D. Witcofski and D. C. Marcum, Jr., “Effect of Thickness and Sweep Angle on the Longitudinal Aerodynamic Characteristics of Slab Delta Planforms at a Mach Number of 20,” *TN-D 3459*, 1966.

[15] M. V. Lowson and A. J. Riley, “Vortex Breakdown Control by Delta-Wing Geometry,” *J. Aircr.*, vol. 32, no. 4, pp. 832–838, 1995.

[16] J. J. Miau, R. C. Chang, J. H. Chou, and C. K. Lin, “Nonuniform Motion of Leading-Edge Vortex Breakdown on Ramp Pitching Delta Wings,” *AIAA J.*, vol. 30, no. 7, pp. 1691–1702, 1992.

[17] J. J. Wang and S. F. Lu, “Effects of Leading-Edge Bevel Angle on the Aerodynamic Forces of a Non-slender 50 Degree Delta Wing,” *Aeronaut. J.*, vol. 109, no. 1098, pp. 403–407, 2005.

[18] M. Nakajima, Y., Nakao, Y., Nakamura, Y., and Yasuhara, “Flow Field Around Thick Delta Wing with Rounded Leading Edge,” *SAE Tech. Pap. 912009*, 1991.

[19] H. Kawazoe, Y. Nakamura, T. Ono, and Y. Ushimaru, “Static and Total Pressure Distributions around a Thick Delta Wing with Rounded Leading Edge,” *AlAA 94-2321, 25th AlAA Plasmadynamics Lasers Conf.*, 1994.

[20] H. Werlé, “Quelques Résultats Expérimentaux Sur les Ailes en Flèche, aux Faibles Vitesses, Obtenus en Tunnel Hydrodynamique,” *La Rech. Aeronaut.*, 1954.

[21] P. B. Earnshaw and J. A. Lawford, “Low-Speed Wind-Tunnel Experiments

on a Series of Sharp-Edged Delta Wings," *Aeronaut. Res. Counc.*, no. 3424, 1964.

[22] J. D. Bird, "Tuft-Grid Surveys at Low Speeds for Delta Wings," *NASA Tech. Note*, 1969.

[23] E. C. Polhamus, "Predictions of Vortex-Lift Characteristics by a Leading-Edge Suction Analogy," *J. Aircr.*, vol. 8, no. 4, pp. 193–199, 1971.

[24] G. Erickson, "Water-Tunnel Studies of Leading-Edge Vortices," vol. 19, no. 6, pp. 442–448, 1981.

[25] T. Benjamin, "Some Developments in the Theory of Vortex Breakdown," *J. Fluid Mech.*, vol. 28, no. 1, pp. 65–84, 1967.

[26] T. B. Benjamin, "Theory of the Vortex Breakdown Phenomenon," vol. 14, pp. 593–623, 1962.

[27] T. Sarpkaya, "Effect of the Adverse Pressure Gradient on Vortex Breakdown," *AIAA J.*, vol. 12, no. 5, pp. 602–607, 1974.

[28] T. Sarpkaya, "On Stationary and Travelling Vortex Breakdowns," *J. Fluid Mech.*, vol. 45, no. 3, p. 545, 1971.

[29] T. Sarpkaya, "Vortex Breakdown in Swirling Conical Flows," *AIAA J.*, vol. 9, no. 9, pp. 1792–1799, 1971.

[30] E. Wedemayer, "Vortex Breakdown," *AGARD High Angle-of-Attack Aerodyn.*, no. 9, p. 1982, 1982.

[31] M. Escudier, "Vortex Breakdown: Observations and Explanations," *Prog. Aerosp. Sci.*, vol. 25, no. 2, pp. 189–229, 1988.

[32] M. Gad-El-Hak and R. F. Blackwelder, "The Discrete Vortices from a Delta Wing," *AIAA J.*, vol. 23, no. 6, pp. 962–963, 1985.

[33] M. V. Ol and M. Gharib, "Leading-Edge Vortex Structure of Nonslender Delta Wings at Low Reynolds Number," *AIAA J.*, vol. 41, no. 1, pp. 16–26,

2003.

[34] R. E. Gordnier and M. R. Visbal, “Compact Difference Scheme Applied to Simulation of Low-Sweep Delta Wing Flow,” *AIAA J.*, vol. 43, no. 8, pp. 1744–1752, 2005.

[35] G. S. Taylor, T. Schnorbus, and I. Gursul, “An Investigation of Vortex Flows Over Low Sweep Delta Wings,” *33rd AIAA Fluid Dyn. Conf. Exhib.*, no. June, pp. 1–13, 2003.

[36] B. Yaniktepe and D. Rockwell, “Flow Structure on a Delta Wing of Low Sweep Angle,” *AIAA J.*, vol. 42, no. 3, pp. 513–523, 2004.

[37] W. Jin-Jun and Z. Wang, “Experimental Investigations on Leading-Edge Vortex Structures for Flow over Non-Slender Delta Wings,” *Chinese Phys. Lett.*, vol. 25, no. 7, pp. 2550–2553, 2008.

[38] I. Gursul, “Unsteady Flow Phenomena Over Delta Wings at High Angle of Attack,” *AIAA J.*, vol. 32, no. 2, pp. 225–231, 1994.

[39] R. E. Gordnier and M. R. Visbal, “Unsteady Vortex Structure over a Delta Wing,” *J. Aircr.*, vol. 31, no. 1, pp. 243–248, 1994.

[40] H. Ashley, J. Katz, M. A. Jarrah, and T. Vaneck, “Survey of Research on Unsteady Aerodynamic Loading of Delta Wings, vol. 5, no. 4, pp. 363–390, Jul. 1991.,” *J. Fluids Struct.*, vol. 5, no. 4, pp. 363–390, 1991.

[41] M. Menke, H. Yang, and I. Gursul, “Experiments on the Unsteady Nature of Vortex Breakdown over Delta Wings,” *Exp. Fluids*, vol. 207, no. 3, pp. 262–272, 1999.

[42] I. Gursul and W. Xie, “Buffeting Flows over Delta Wings,” *AIAA J.*, vol. 37, no. 1, 1999.

[43] R. C. Nelson and A. Pelletier, “The Unsteady Aerodynamics of Slender Wings and Aircraft Undergoing Large Amplitude Maneuvers,” *Prog. Aerosp. Sci.*, vol. 39, no. 2–3, pp. 185–248, 2003.

[44] G. S. Taylor and I. Gursul, “Buffeting Flows over a Low-Sweep Delta Wing,” *AIAA J.*, vol. 42, no. 9, pp. 1737–1745, 2004.

[45] M. M. Yavuz, M. Elkhoury, and D. Rockwell, “Near-Surface Topology and Flow Structure on a Delta Wing,” *AIAA J.*, vol. 42, no. 2, pp. 332–340, 2004.

[46] İ. Öztürk, “Experimental Analysis of Flow Structure on Moderate Sweep Delta Wing,” p. M.S. thesis, Dept. Mech. Eng. Dept., METU., Ankara.

[47] M. Zharfa, I. Ozturk, and M. M. Yavuz, “Flow Structure on Nonslender Delta Wing: Reynolds Number Dependence and Flow Control,” *AIAA J.*, vol. 54, no. 3, pp. 880–897, 2016.

[48] P. B. Earnshaw, “An Experimental Investigation of the Structure of a Leading Edge Vortex,” *R.A.E. Tech. Note*, no. Aero 2740, 1961.

[49] M. Ozgoren, B. Sahin, and D. Rockwell, “Vortex Structure on a Delta Wing at High Angle of Attack,” *AIAA J.*, vol. 40, no. 2, pp. 285–292, 2002.

[50] A. J. Riley and M. V. Lowson, “Development of a Three-Dimensional Free Shear Layer,” vol. 369, pp. 49–89, 1998.

[51] M. G. Hall, “Vortex Breakdown,” *Annu. Rev. Fluid Mech.*, vol. 4, no. 1, pp. 195–218, 1972.

[52] O. Lucca-Negro and T. O’Doherty, “Vortex Breakdown: A Review,” *Prog. Energy Combust. Sci.*, vol. 27, no. 4, pp. 431–481, 2001.

[53] Y.-C. Liu and F.-B. Hsiao, “Aerodynamic Investigations of Low-Aspect-Ratio Thin Plate Wings at Low Reynolds Numbers,” *J. Mech.*, vol. 28, no. 1, pp. 77–89, 2012.

[54] M. V. Lowson, “Some Experiments with Vortex Breakdown (Water Tunnel Flow Visualization on Slender Delta Wings Reveal Vortex Breakdown Formation to Be a Nonaxisymmetric,” *R. Aeronaut. Soc. J.*, 1964.

[55] M. M. Yavuz, “Origin and Control of the Flow Structure and Topology on

Delta Wings," p. Ph.D. dissertation, Dept. Mech. Eng. and Mechanics, 2005.

[56] A. Honkan and J. Andreopoulos, "Instantaneous Three-Dimensional Vorticity Measurements in Vortical Flow over a Delta Wing," *AIAA J.*, vol. 35, no. 10, pp. 1612–1620, 1997.

[57] D. Peake and M. Tobak, "Three-Dimensional Separation and Reattachment," *AGARD High Angle-of-Attack Aerodyn.*, 1982.

[58] L. E. Ericsson and M. View, "Effect of Leading-Edge Cross-Sectional Shape on Nonslender Wing Rock," *J. Aircr.*, vol. 40, no. 2, pp. 407–410, 2003.

[59] J. M. Délery, "Robert Legendre and Henri Werlé: Toward the Elucidation of Three-Dimensional Separation," *Annu. Rev. Fluid Mech.*, vol. 33, no. 1, pp. 129–154, 2001.

[60] H. Werle, "Bursting of Conical Vortex Sheet above Delta Wing Surface at Low Speeds," *La Rech. Aeronaut.*, no. 74, pp. 25–30, 1960.

[61] S. Y. Ruo and J. G. Theisen, "Calculation of Unsteady Transonic Aerodynamics for Oscillating Wings with Thickness," vol. 11, no. 10, pp. 601–608, 1975.

[62] C. Shih and Z. Ding, "Trailing-Edge Jet Control of Leading-Edge Vortices of a Delta Wing," *AIAA J.*, vol. 34, no. 7, pp. 1447–1457, 1996.

[63] H. Golparvar, S. Irani, and M. Mousavi Sani, "Experimental Investigation of Linear and Nonlinear Aeroelastic Behavior of a Cropped Delta Wing with Store in Low Subsonic Flow," *J. Brazilian Soc. Mech. Sci. Eng.*, vol. 38, no. 4, pp. 1113–1130, 2016.

[64] J. Saltzman and T. G. Ayers, "Review of Flight-to-Wind-Tunnel Drag Correlation Edwin," *J. Aircr.*, vol. 19, no. 10, pp. 801–811, 1982.

[65] D. Tang, J. K. Henry, and E. H. Dowell, "Limit cycle oscillations of delta wing models in low subsonic flow," *AIAA J.*, vol. 37, no. 11, pp. 1355–1362, 1999.

[66] A. McClain, Z.-J. Wang, E. Vardaki, and I. Gursul, “Unsteady aerodynamics of free-to-roll non-slender delta wings,” *45th AIAA Aerosp. Sci. Meet. Exhib. Reno, NV, AIAA Pap.*, vol. 1074, pp. 1–14, 2007.

[67] N. Lambourne and D. W. Bryer, “The Bursting of Leading-Edge Vortices-Some Observations and Discussion of the Phenomenon,” *Aeronaut. Res. Counc.*, vol. 3282, pp. 1–35, 1961.

[68] S. J. Kline and F. A. McClintock, “Describing Uncertainties in Single-Sample Experiments,” *Mech. Eng.*, p. p.3.

[69] *INSIGHT 4G TM GLOBAL IMAGE , ACQUISITION , ANALYSIS , & DISPLAY SOFTWARE*. 2015.

APPENDIX A

SOURCE CODES FOR PRESSURE COEFFICIENT CALCULATION

```
clear all
clc



%=======Uncertainty Calculation=================
P_w=-31.31128721;       %%Pa (Static Pressure on the Wing)
P_inf=-22.87358627;     %%Pa (Static Pressure of the Free Stream)
P_stag=-10.81869585;     %%Pa (Stagnation Pressure of the Free
Stream
P_r=0.075;          %%Pa (Measurement Resolution of the Device
(0.003% FS))


Span=0.3;          %%m  (Wing Span, Measured with ruler)
Chord=0.105;        %%m  (Wing Chord, Measured with rules)
d_rul=0.001        %%m  (Resolution of ruler)
As=0.5*Span*Chord; %%m^2(Wing Surface Area)

%=============================================
%Uncertainty of Dynamic Pressure

P_dyn=P_stag-P_inf;
dPdyn_Pstag=1;
dPdyn_Pinf=-1;
dPdyn=((dPdyn_Pstag*P_r)^2+(dPdyn_Pinf*P_r)^2)^0.5

Urel_dPdyn=dPdyn/P_dyn   % (Relative uncertainty of Dynamic
Pressure)

%=============================================

%=============================================
%Uncertainty of Wing Surface Area
dAs_sp=0.5*Chord;
dAs_ch=0.5*Span;
dAs=((dAs_sp*d_rul)^2+(dAs_ch*d_rul)^2)^0.5;

Urel_dAs=dAs/As   % (Relative uncertainty of Wing Surface Area)
```

```
%=============================================
%Uncertainty of Pressure Coefficient

Cp=(P_w-P_inf)/(P_stag-P_inf);

dCp_Pw=1/(P_stag-P_inf);
dCp_Pinf=(P_w-P_stag)/(P_inf-P_stag)^2;
dCp_Pstag=(P_inf-P_w)/(P_inf-P_stag)^2;

dCp=((dCp_Pw*P_r)^2+(dCp_Pinf*P_r)^2+(dCp_Pstag*P_r)^2)^0.5

Urel_Cp=dCp/-Cp % (Relative uncertainty of Pressure Coefficient)

%=============================================
```

APPENDIX B

SURFACE AND CROSS FLOW SMOKE VISUALIZATIONS FOR THICKNESS-TO-CHORD RATIOS AS 0.0475, 0.095, 0.1425, 0.19 α=10° FOR RE=10000 & AT α=4°, 6°, 8° AND 10° FOR RE=35000

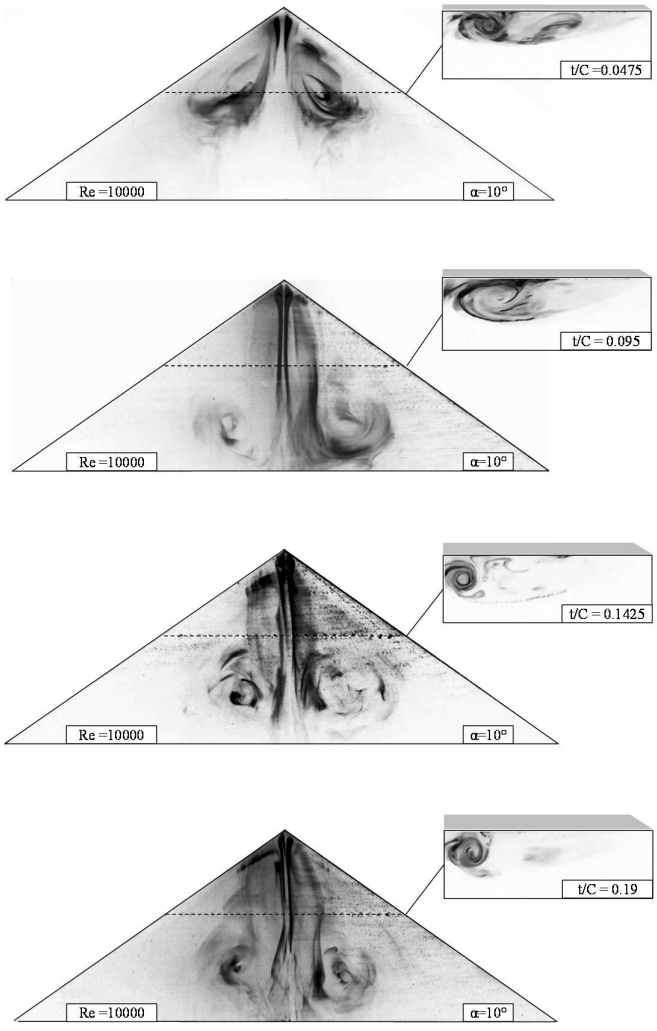

B.1 Surface and cross flow smoke visualizations for all wings at α= 10° for Re=10000

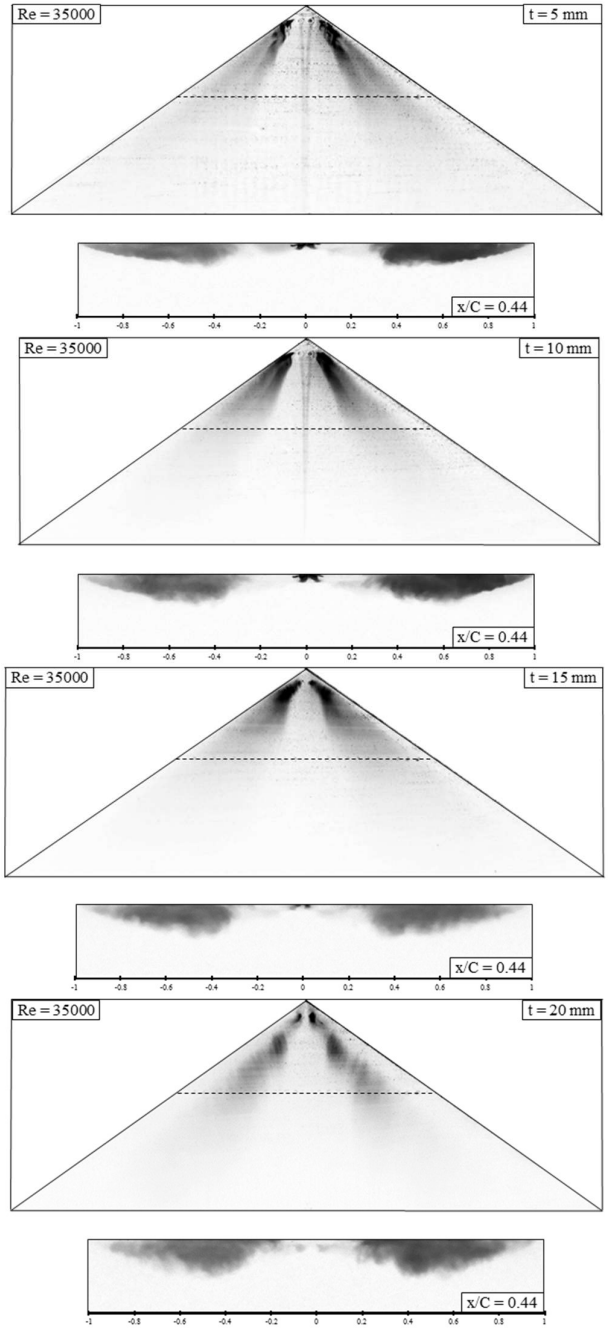

B.2 Surface and cross flow smoke visualizations for all wings at α= 4° for Re=35000

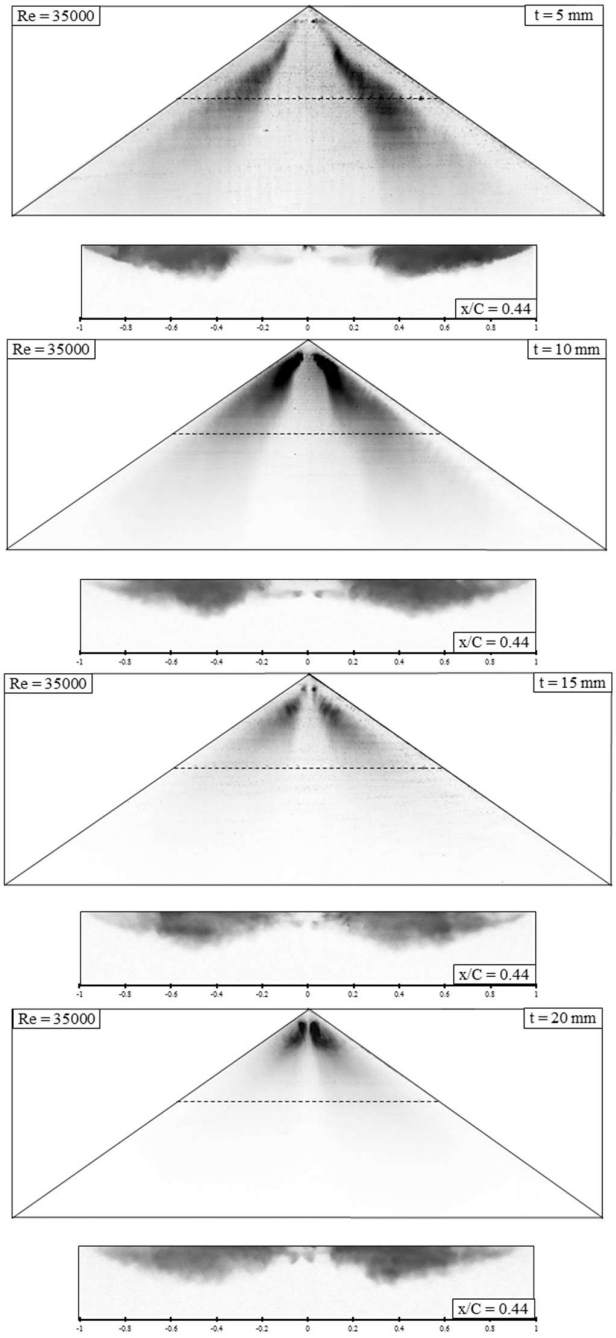

B.3 Surface and cross flow smoke visualizations for all wings at α= 6° for Re=35000

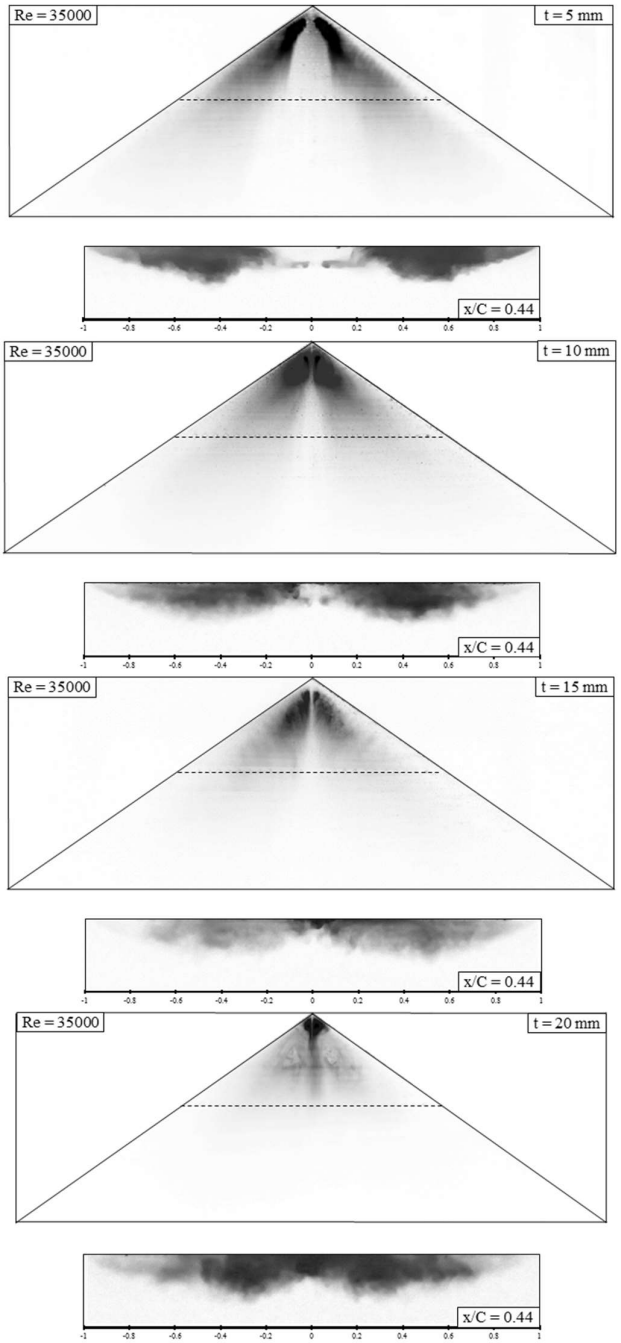

B.4 Surface and cross flow smoke visualizations for all wings at α= 8° for Re=35000

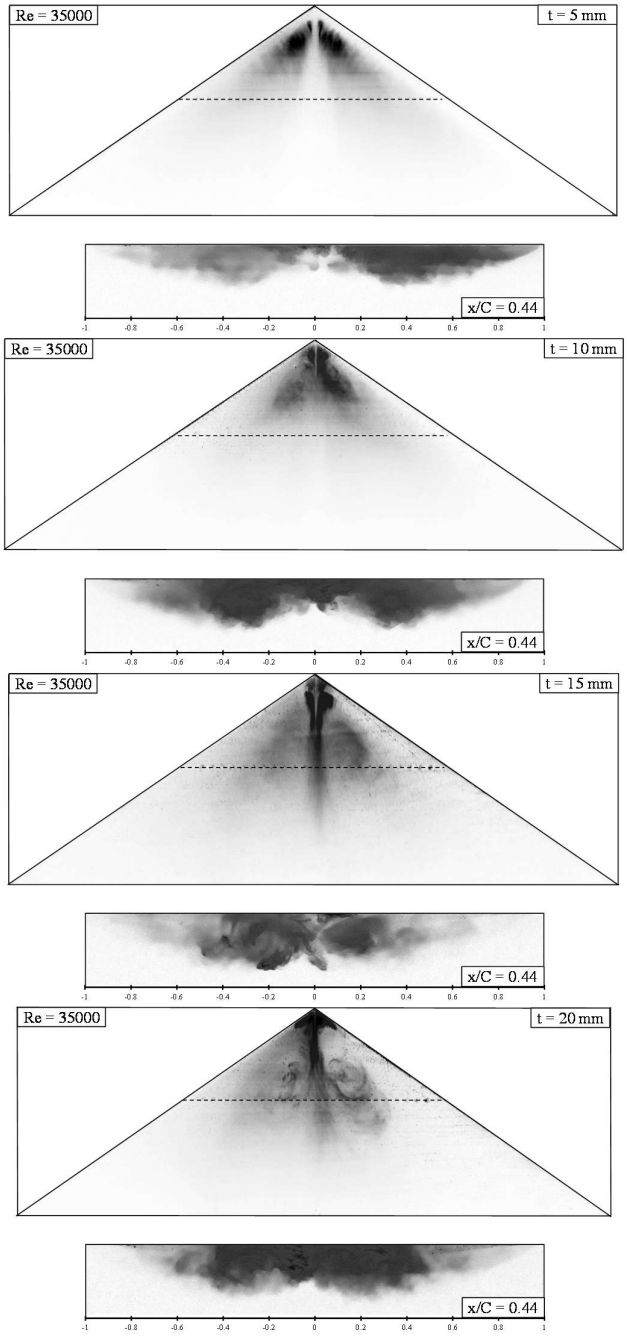

B.5 Surface and cross flow smoke visualizations for all wings at α= 10° for Re=35000

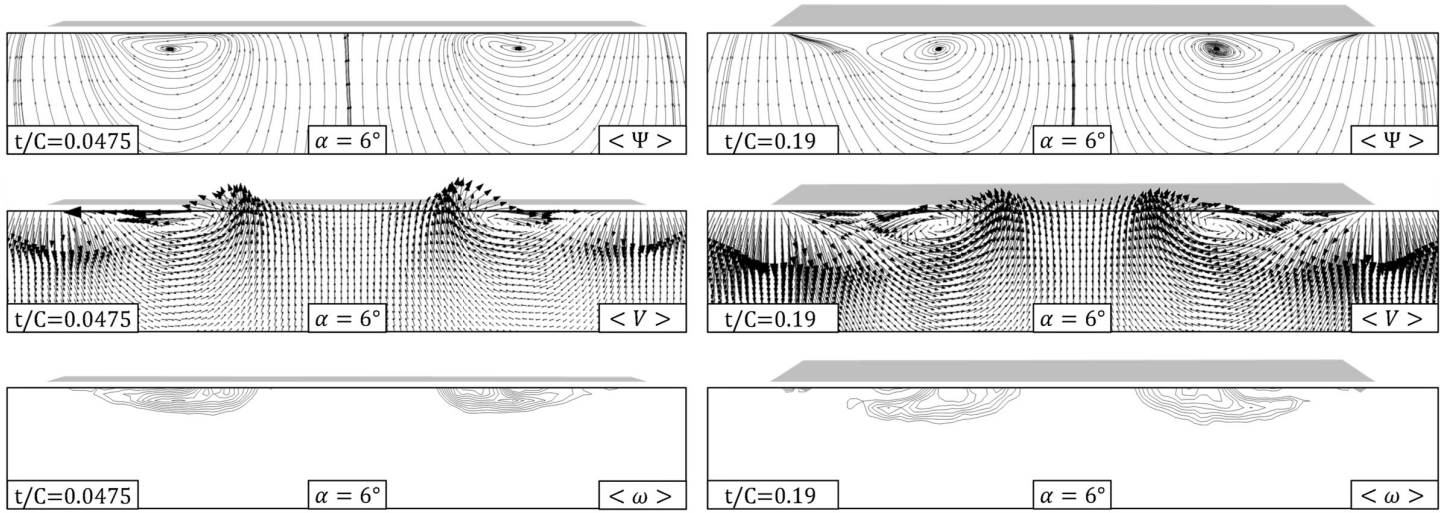

B.6 Patterns of time-averaged velocity vectors $\langle \boldsymbol{V} \rangle$, streamlines $\langle \boldsymbol{\Psi} \rangle$ and constant contours of axial vorticity $\langle \boldsymbol{\omega} \rangle$ of cross flow PIV at angle of attack α=6° for Re=35000: $[|\langle \omega \rangle|]_{min}$=200 s^{-1}, $\Delta[|\langle \omega \rangle|]$=100 s^{-1}

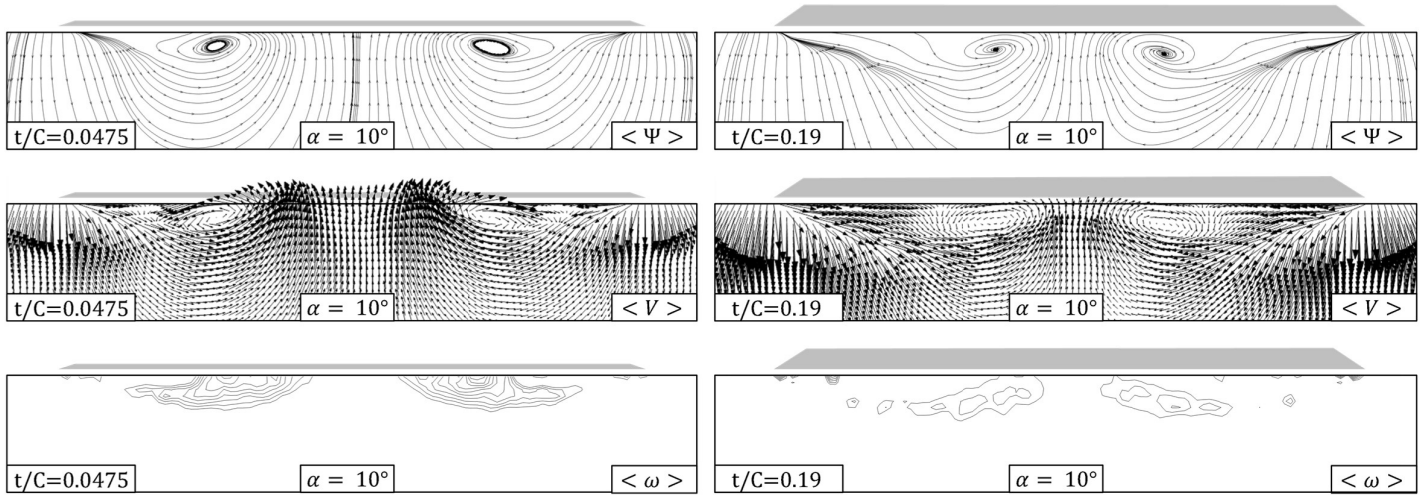

B.7 Patterns of time-averaged velocity vectors $\langle \boldsymbol{V} \rangle$, streamlines $\langle \boldsymbol{\Psi} \rangle$ and constant contours of axial vorticity $\langle \boldsymbol{\omega} \rangle$ of cross flow PIV at angle of attack α=10° for Re=35000: $[|\langle\omega\rangle|]_{min}$=200 s^{-1}, $\Delta[|\langle\omega\rangle|]$=100 s^{-1}

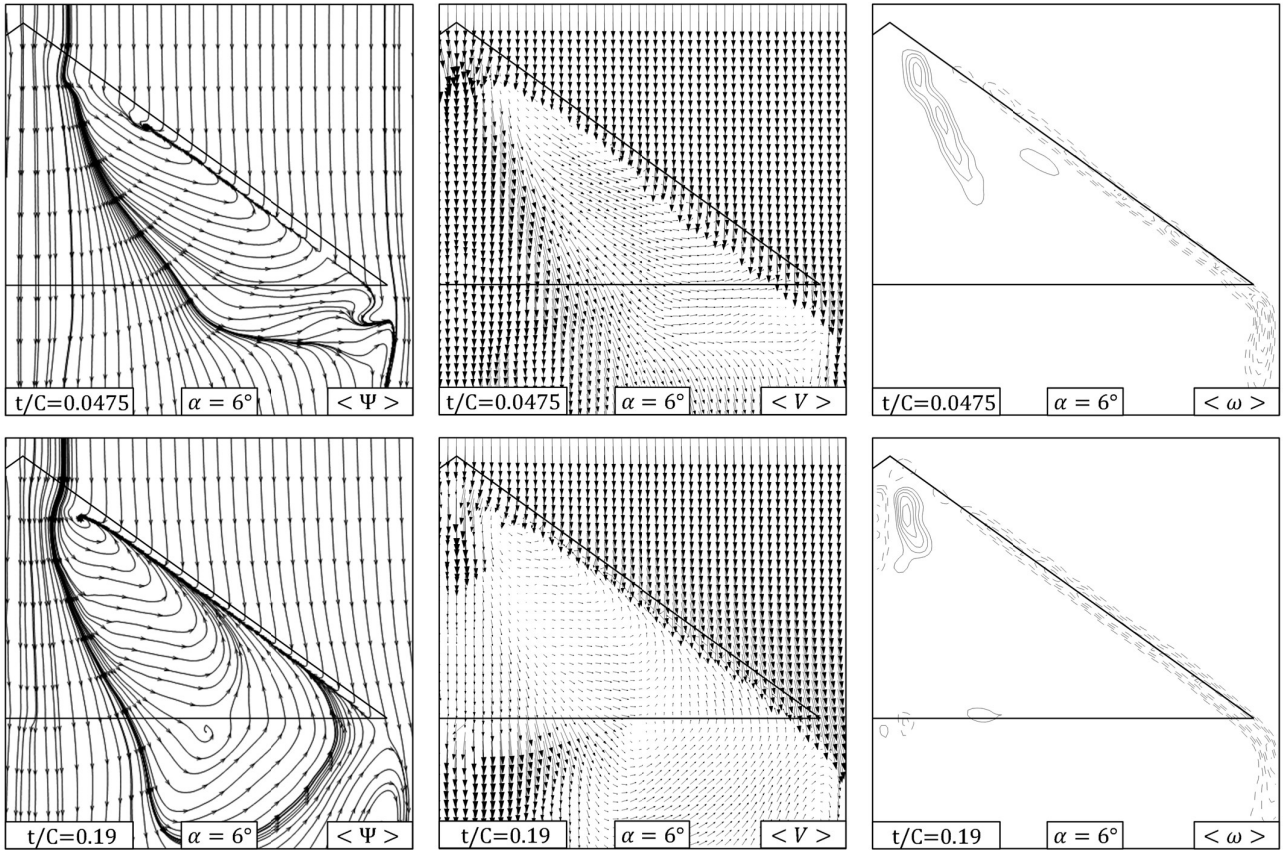

B.8 Patterns of time-averaged velocity vectors $\langle \boldsymbol{V} \rangle$, streamlines $\langle \boldsymbol{\Psi} \rangle$ and constant contours of surface normal vorticity $\langle \boldsymbol{\omega} \rangle$ of surface flow PIV at angle of attack α=6° for Re=35000: $[|\langle \omega \rangle|]_{min}$=200 s^{-1}, $\Delta[|\langle \omega \rangle|]$=100 s^{-1}

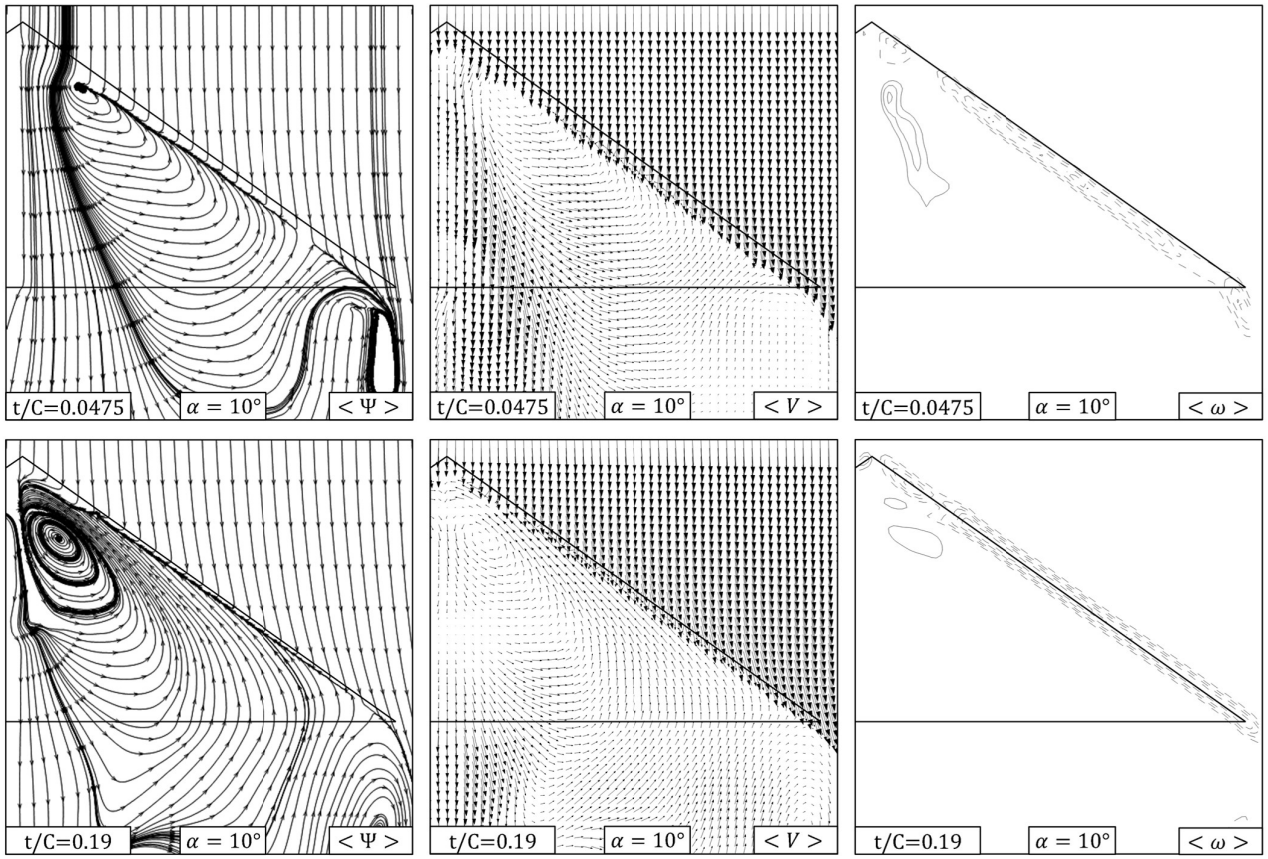

B.9 Patterns of time-averaged velocity vectors $\langle \boldsymbol{V} \rangle$, streamlines $\langle \boldsymbol{\Psi} \rangle$ and constant contours of surface normal vorticity $\langle \boldsymbol{\omega} \rangle$ of surface flow PIV at angle of attack α=10° for Re=35000: $[|\langle \omega \rangle|]_{min}$=200 s^{-1}, $\Delta[|\langle \omega \rangle|]$=100 s^{-1}